Journal of Sound and Vibration (2002) **249**(4), 743–773
doi:10.1006/jsvi.2001.3911, available online at http://www.idealibrary.com on IDEAL®

NON-LINEAR MODELLING OF ROTOR DYNAMIC SYSTEMS WITH SQUEEZE FILM DAMPERS—AN EFFICIENT INTEGRATED APPROACH

P. BONELLO, M. J. BRENNAN AND R. HOLMES

Institute of Sound and Vibration Research, University of Southampton, Southampton,
SO 17 1*BJ, England. E-mail: ppb@isvr.soton.ac.uk*

(*Received* 27 *April* 2001, *and in final form* 10 *July* 2001)

Squeeze film dampers used in rotor assemblies such as aero-engines introduce non-linear damping forces into an otherwise linear rotor dynamic system. The steady state periodic response of such rotor dynamic systems to rotating out-of-balance excitation can be efficiently determined by using periodic solution techniques. Such techniques are essentially faster than time marching techniques. However, the computed periodic solutions need to be tested for stability and recourse to time marching is necessary if no periodic attractor exists. Hence, an efficient integrated approach, as presented in this paper, is necessary. Various techniques have been put forward in order to determine the periodic solutions, each with its own advantages and disadvantages. In this paper, a receptance harmonic balance method is proposed for such a purpose. In this method, the receptance functions of the rotating linear part of the system are used in the non-linear analysis of the complete system. The advantages of this method over current periodic solution techniques are two-fold: it results in a compact model, and the receptance formulation gives the designer the widest possible choice of modelling techniques for the linear part. Stability of these periodic solutions is efficiently tested by applying Floquet Theory to the modal equations of the system and time marching carried out on these equations, when necessary. The application of this integrated approach is illustrated with simulations and an experiment on a test rig. Excellent correlation was achieved between the periodic solution approach and time marching. Good correlation was also achieved with the experiment.

1. INTRODUCTION

Squeeze film dampers are widely used in rotor assemblies, particularly aero-engines, to stabilize and/or attenuate vibrations and transmitted forces [1]. These elements introduce non-linear damping forces into an otherwise linear rotor dynamic system. Figure 1 shows a schematic of a squeeze film damper (SFD). The "journal" refers to the outer race of a rolling-element bearing mounted on the shaft. The journal is prevented from rotating but is free to orbit in an oil-filled annular clearance in the bearing housing, forming the SFD. A retaining spring is optionally placed in parallel with the squeeze film. This serves to support the static load on the journal and to prevent it from rotating. Static misalignments of the journal centre J from the housing centre B aggravate the non-linear effects, resulting in non-circular orbits and increasing the likelihood of non-synchronous vibration [2]. In the absence of a retainer spring, the journal is prevented from rotating by anti-rotation pins or dogs. In such a case, the squeeze film performs the additional function of a bearing. However, it cannot support a static load in the absence of a dynamic load and the vibration is highly non-linear.

0022-460X/02/040743 + 31 $35.00/0

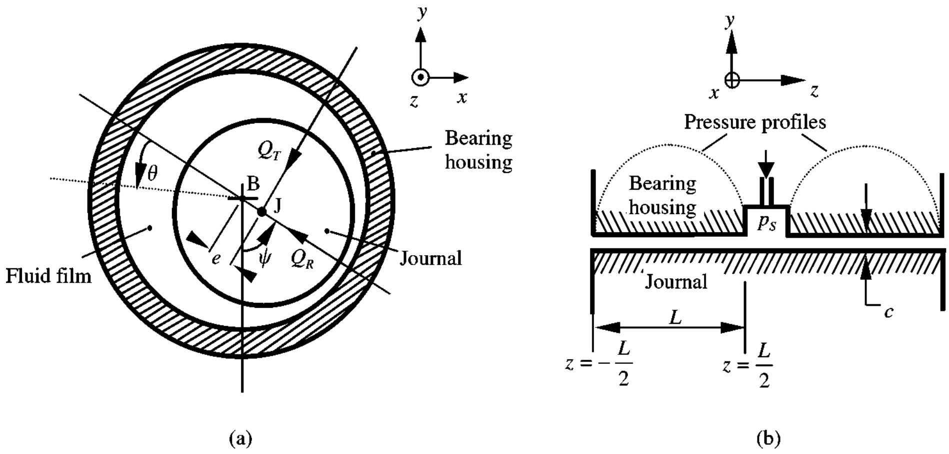

Figure 1. Sections through squeeze film damper: (a) transverse cross-section; (b) axial cross-section.

The techniques used for the determination of the unbalance response of squeeze film damped rotor dynamic systems can be broadly divided into two categories: periodic solution techniques and time marching methods. Periodic solution techniques employ analytical methods like the harmonic balance method [1, 3] or the analogous trigonometric collocation method [2, 4], to determine equilibrium (i.e., *steady state*) periodic solutions of assumed fundamental period. These solutions can be either stable (attractors) or unstable (repellors). The latter are unattainable in practice due to inevitable minor fluctuations in operating conditions. Time marching methods [5] involve numerical integration of the system equations from given initial conditions over sufficiently long integration times for transients to die out and a stable equilibrium solution (attractor) to be reached which is not necessarily periodic. While periodic solution techniques are essentially much faster than time marching methods, the solutions thus obtained need to be tested for stability and recourse to time marching necessary if no *periodic* attractor exists. In fact, quasi-periodic and chaotic attractors are possible in squeeze film damped systems [2, 6]. Hence, the aim of this paper is to present an efficient integrated approach to the determination of the non-linear response, encompassing a periodic solution technique, stability analysis and time marching. Such an integrated non-linear modelling approach is of much practical importance since non-synchronous vibration of both the periodic and aperiodic type promotes cyclic stresses, aggravating fatigue problems.

Various techniques have been put forward in order to determine the steady state periodic response of squeeze film damped systems, each with its own advantages and disadvantages. The common strategy is to regard the forces from the non-linear elements as external, acting on the rotating linear part, which is usually modelled by the finite element (FE) technique. In references [1–3] the harmonic balance method or the trigonometric collocation method is applied to the FE equations of the system, resulting in a set of non-linear algebraic equations. A condensation technique, involving the inversion of large FE matrices, is then applied to reduce the number of unknown degrees of freedom to the number of non-linear degrees of freedom. The stability of the response is then tested (see references [1, 2]) by applying Floquet Theory to the FE equations, again resulting in large matrices. Such FE-based periodic solution and stability techniques are clearly impractical for large systems. In reference [4], a component mode synthesis approach is adopted. The trigonometric collocation method is applied to the modal equations of the system, making the technique tractable for large order systems. This requires the solution of the eigenproblem of the rotating linear part and modal truncation. However, as observed in reference [3], this needs to be done at each rotational speed if gyroscopic effects are significant.

As regards the time marching methods, modal analysis over a limited number of modes [5] is the only viable approach. In reference [5], the transient response of a squeeze film damped rotating system is computed by numerically integrating the modal equations.

In this paper, a *receptance harmonic balance method* is proposed for the determination of the periodic solutions to the unbalance response problem. Harmonic balance principles are applied to the receptance model of the rotating linear part. The required non-linear algebraic equations are easily extracted in the frequency domain, without any costly condensation, resulting in a compact model. The receptance functions can be computed by using any convenient linear rotor dynamic modelling technique. The designer is free to use any of the various frequency-based modelling techniques that have been proposed as efficient alternatives to FE for the computation of the harmonic response of linear rotating systems, such as transfer matrices (TM), mechanical impedance (MI, or analogously, dynamic stiffness), and hybrids like TM/FE, MI/FE [7]. The receptance formulation does not restrict the designer to the exclusive use of TM as in reference [8], making the proposed technique effective at including the dynamics of the rotor support structure. The stability of the periodic solutions is efficiently tested by applying Floquet Theory to a limited number of the modal equations of the system. This original method for stability determination is more tractable to large order systems than the alternative methods presented in references [1, 2]. Time marching is also carried out on the modal equations, when necessary.

Following this introduction, the integrated non-linear modelling technique is developed (section 2). It is then applied to a test rig and validated with simulations and experiment (section 3). (A list of Nomenclature is given in Appendix A.)

2. GENERAL THEORY

2.1. MODEL DESCRIPTION

The general model is shown in Figure 2(a). n_{SFD} squeeze film dampers are fitted between positions J_i and B_i, $i = 1 \cdots n_{SFD}$, on the rotor and support structure respectively. J_i refers to

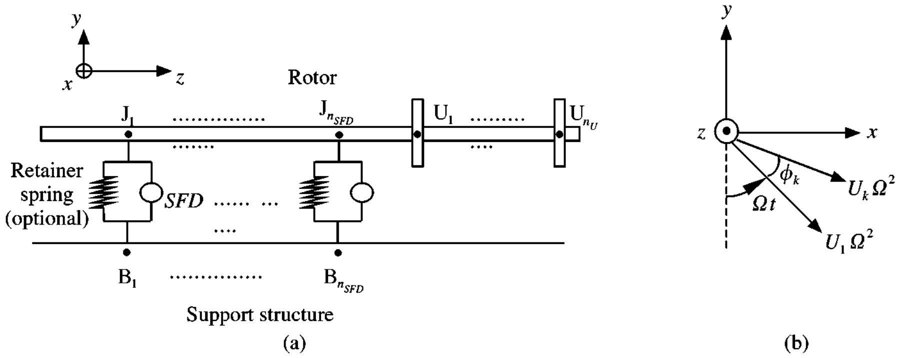

Figure 2. Schematic of squeeze film damped rotor dynamic system: (a) general model; (b) rotating out-of-balance forces.

the journal centre and B_i to the bearing housing centre at SFD no. i. A retainer spring can be optionally placed between J_i and B_i. The support structure is in general non-rigid, exhibiting dynamic behaviour. Note that the rotor and support structure may be linearly connected at locations other than those of the SFDs. However, these linear connections are not shown in Figure 2(a). The model can additionally accommodate linear (viscous) damping forces but material (hysteretic) damping is neglected. The unbalance forces are assumed to be concentrated at discs located at points U_k, $k = 1 \cdots n_U$, along the rotor and are given by (Figure 2(b))

$$P_{xk} = U_k \Omega^2 \sin(\Omega t + \phi_k), \qquad P_{yk} = -U_k \Omega^2 \cos(\Omega t + \phi_k), \tag{1a, b}$$

where Ω (rad/s) is the rotational speed. Unbalance moments due to incorrect fixing of the discs can be additionally considered. These will also be harmonic functions of the circular frequency Ω [9].

With reference to Figure 1(a), the squeeze film forces Q_x, Q_y in the x, y directions, respectively, on a journal J are given by resolving the radial and tangential forces Q_R, Q_T:

$$Q_x = -\{Q_R(\varepsilon, \psi, \dot{\varepsilon}, \dot{\psi}) \sin\psi + Q_T(\varepsilon, \psi, \dot{\varepsilon}, \dot{\psi}) \cos\psi\}, \tag{2a}$$

$$Q_y = Q_R(\varepsilon, \psi, \dot{\varepsilon}, \dot{\psi}) \cos\psi - Q_T(\varepsilon, \psi, \dot{\varepsilon}, \dot{\psi}) \sin\psi. \tag{2b}$$

In these equations, $\varepsilon = e/c$ is the non-dimensional eccentricity of the journal centre, where c is the radial clearance of the damper, and ψ is the attitude angle. Note that, in line with standard SFD modelling practice, it is implicitly assumed that the journal assembly is radially rigid with respect to the oil film. The forces Q_R, Q_T are obtained by spatially integrating the instantaneous pressure distribution $p(\theta, z)$ within the squeeze film after truncating it below a minimum pressure p_c at which the film is assumed to rupture (cavitate). For an unsealed damper with two lands of length L each, separated by a deep groove through which oil is supplied at pressure p_S (see Figure 1(b)), the distribution $p(\theta, z)$ is given by the short bearing approximation [10]:

$$p(\theta, z) = \frac{6\eta}{c^2} \frac{\{\varepsilon\dot{\psi}\sin\theta + \dot{\varepsilon}\cos\theta\}}{\{1 + \varepsilon\cos\theta\}^3}\left(z^2 - \frac{L^2}{4}\right) + p_s\left(\frac{z}{L} + \frac{1}{2}\right). \tag{3}$$

Q_R, Q_T are hence computed as

$$Q_R = -2R\int_{-L/2}^{L/2}\int_0^{2\pi} p_m(\theta, z)\cos\theta\, \mathrm{d}\theta\, \mathrm{d}z, \; Q_T = -2R\int_{-L/2}^{L/2}\int_0^{2\pi} p_m(\theta, z)\sin\theta\, \mathrm{d}\theta\, \mathrm{d}z. \tag{4a, b}$$

In these equations, $p_m(\theta, z)$ is a modified pressure distribution defined as

$$p_m(\theta, z) = \begin{Bmatrix} p(\theta, z), & p(\theta, z) > p_c \\ p_c, & p(\theta, z) \leqslant p_c \end{Bmatrix}. \tag{5}$$

The cavitation pressure p_c is taken as $-101{\cdot}325$ kPa (absolute zero pressure) [11]. In Figure 2(a), the squeeze film forces on J_i, $i = 1 \cdots n_{SFD}$, in the x and y directions are Q_{xi}, Q_{yi}, while those on B_i are $-Q_{xi}$, $-Q_{yi}$, since the inertia of the fluid film is neglected. Q_{xi}, Q_{yi} are non-linear functions of the *relative* displacements and velocities across the damper.

The *remnant linear subsystem* is defined as the system in Figure 2(a) minus the squeeze film dampers. Let $\mathbf{u}$ and $\mathbf{f}$ be, respectively, the corresponding $(P \times 1)$ vectors of the instantaneous degrees of freedom and instantaneous external forces/moments. In general, there will be four "non-linear" degrees of freedom associated with each damper location: X_{J_i}, Y_{J_i}, X_{B_i}, Y_{B_i} (absolute displacements of J_i, B_i in x, y directions). However, if the support structure is rigid (i.e., X_{B_i}, $Y_{B_i} = 0$) this number is reduced to two. It should be noted that, while P is arbitrarily large, the vector $\mathbf{f}$ will be sparse, containing only a finite number of non-zero elements, depending on the number of forces/moments that are taken to be external to the remnant subsystem. This force vector is divided into two component vectors as

$$\mathbf{f} = \mathbf{f}(\mathbf{u}_N, \dot{\mathbf{u}}_N, t) = \begin{bmatrix} \mathbf{f}_N(\mathbf{u}_N, \dot{\mathbf{u}}_N) \\ \mathbf{0} \end{bmatrix} + \mathbf{f}_R(t), \tag{6}$$

where $\mathbf{f}_N$ is the $(P_N \times 1)$ vector of motion-dependent forces/moments and $\mathbf{u}_N$ the $(P_N \times 1)$ vector of the associated degrees of freedom. The $(P \times 1)$ vector $\mathbf{f}_R$ contains the unbalance forces, unbalance moments (if any) and static loads (if taken into account) at the appropriate rows, and zeros elsewhere. The vector $\mathbf{u}$ is ordered and partitioned in accordance with equation (6):

$$\mathbf{u} = \begin{bmatrix} \mathbf{u}_N \\ \mathbf{u}_L \end{bmatrix}, \tag{7}$$

where $\mathbf{u}_L$ is a $(P_L \times 1)$ vector.

2.2. RECEPTANCE HARMONIC BALANCE (RHB) ANALYSIS

In the RHB approach, the vector $\mathbf{f}_N$ comprises the squeeze film forces only. Hence, in this analysis, $P_N = 4n_{SFD}$ for a flexible support structure, while for a rigid support structure, $P_N = 2n_{SFD}$. The dynamics at excitation frequency ω (rad/s) of the rotating remnant linear subsystem are modelled by a $(P \times P)$ receptance matrix $\mathbf{R}(\omega, \Omega)$ of frequency response functions, given by

$$\tilde{\mathbf{u}} = \mathbf{R}(\omega, \Omega)\,\tilde{\mathbf{f}}. \tag{8}$$

$\tilde{\mathbf{u}}$ and $\tilde{\mathbf{f}}$ are the complex amplitude vectors of $\mathbf{u}$ and $\mathbf{f}$ *i.e., for harmonic excitation at frequency* ω, $\mathbf{u}$ and $\mathbf{f}$ are given by

$$\mathbf{u} = \mathrm{Re}\left\{\tilde{\mathbf{u}}\mathrm{e}^{\mathrm{j}\omega t}\right\} = \mathbf{u}_C \cos\omega t + \mathbf{u}_S \sin\omega t, \quad \mathbf{f} = \mathrm{Re}\left\{\tilde{\mathbf{f}}\mathrm{e}^{\mathrm{j}\omega t}\right\} = \mathbf{f}_C \cos\omega t + \mathbf{f}_S \sin\omega t. \tag{9a, b}$$

In general, $\mathbf{R}$ includes gyroscopic and linear damping terms and hence it is complex, non-symmetric, and dependent on the rotational speed Ω as well as the vibration frequency ω. By manipulating equations (8, 9a,b), the complex numbers can be eliminated from equation (8), resulting in the following pair of equations:

$$\mathbf{u}_C = \mathbf{R}^R(\omega, \Omega)\,\mathbf{f}_C + \mathbf{R}^I(\omega, \Omega)\,\mathbf{f}_S, \quad \mathbf{u}_S = -\mathbf{R}^I(\omega, \Omega)\,\mathbf{f}_C + \mathbf{R}^R(\omega, \Omega)\,\mathbf{f}_S. \tag{10a, b}$$

In equation (10a, b) the superscripts ^{R}, ^{I} respectively, denote the real and imaginary parts of $\mathbf{R}$.

Equilibrium periodic solutions of fundamental frequency ϖ are sought where

$$\varpi = \Omega/N, \quad N \geqslant 1. \tag{11}$$

Hence, $\mathbf{u}$ and $\mathbf{f}$ can be expressed as Fourier series expansions:

$$\mathbf{u} = \bar{\mathbf{u}} + \sum_{s=1}^{m} (\mathbf{u}_C^s \cos s\varpi t + \mathbf{u}_S^s \sin s\varpi t), \quad \mathbf{f} = \bar{\mathbf{f}} + \sum_{s=1}^{m} (\mathbf{f}_C^s \cos s\varpi t + \mathbf{f}_S^s \sin s\varpi t). \tag{12a, b}$$

For computational reasons, only a finite number of harmonics m can be considered. Hence, the solutions sought are essentially approximate. Static loads need not be considered in $\mathbf{f}$ if the elements in vectors $\mathbf{u}_N$ and $\mathbf{u}_L$ in equation (7) are measured from the static condition

$$\mathbf{u}_N = \mathbf{h} - \mathbf{h}_0, \quad \mathbf{u}_L = \mathbf{g}, \tag{13a, b}$$

where $\mathbf{h}$ $(P_N \times 1)$ is the vector of the "non-linear" degrees of freedom at the SFD locations, each measured from the static position of the respective bearing housing centreline. $\mathbf{h}_0$ is the static value of $\mathbf{h}$ and contains zeros for the degrees of freedom of the bearing housings. The remaining rows in $\mathbf{h}_0$ contain the static misalignments of the journals in their respective housings. The $(P_L \times 1)$ vector $\mathbf{g}$ contains the dynamic displacements at the remaining P_L degrees of freedom. The receptance matrix $\mathbf{R}$ is partitioned in a similar manner to $\mathbf{u}$ in equation (7),

$$\mathbf{R} = \begin{bmatrix} \mathbf{S} \\ \mathbf{T} \end{bmatrix}, \tag{14}$$

where the matrices $\mathbf{S}$ and $\mathbf{T}$ are of dimension $(P_N \times P)$ and $(P_L \times P)$ respectively. Equations (10a, b) can now be applied in partitioned form to each of the Fourier coefficient vectors of the dynamic displacements $\mathbf{u}_N = \mathbf{h} - \mathbf{h}_0$, $\mathbf{u}_L = \mathbf{g}$:

$$\bar{\mathbf{h}} - \mathbf{h}_0 = \mathbf{S}_0 \bar{\mathbf{f}}, \tag{15a}$$

$$\mathbf{h}_C^s = \mathbf{S}^R (s\varpi, \Omega)\, \mathbf{f}_C^s + \mathbf{S}^I (s\varpi, \Omega)\, \mathbf{f}_S^s, \; s = 1 \cdots m, \tag{15b}$$

$$\mathbf{h}_S^s = -\mathbf{S}^I (s\varpi, \Omega)\, \mathbf{f}_C^s + \mathbf{S}^R (s\varpi, \Omega)\, \mathbf{f}_S^s, \; s = 1 \cdots m, \tag{15c}$$

$$\bar{\mathbf{g}} = \mathbf{T}_0 \bar{\mathbf{f}}, \tag{16a}$$

$$\mathbf{g}_C^s = \mathbf{T}^R (s\varpi, \Omega)\, \mathbf{f}_C^s + \mathbf{T}^I (s\varpi, \Omega)\, \mathbf{f}_S^s, \; s = 1 \cdots m, \tag{16b}$$

$$\mathbf{g}_S^s = -\mathbf{T}^I (s\varpi, \Omega)\, \mathbf{f}_C^s + \mathbf{T}^R (s\varpi, \Omega)\, \mathbf{f}_S^s, \; s = 1 \cdots m. \tag{16c}$$

In equations (15, 16), $\bar{\mathbf{h}}$, $\mathbf{h}_C^s$, $\mathbf{h}_S^s$ are the Fourier coefficients of $\mathbf{h}$ (as in equations (12)) and $\bar{\mathbf{g}}$, $\mathbf{g}_C^s$, $\mathbf{g}_S^s$ are those of $\mathbf{g}$. Also, $\mathbf{S}_0$, $\mathbf{T}_0$ contain the zero frequency receptances and are real and independent of rotational speed.

Equations (15) define a set of $P_N(2m+1)$ non-linear algebraic equations in an equal number of unknowns contained in $\bar{\mathbf{h}}$, $\mathbf{h}_C^s$, $\mathbf{h}_S^s$. The unknowns in these vectors are grouped into one $P_N(2m+1) \times 1$ vector $\mathbf{v}$ and the system in equations (15) is written in the form

$$\mathbf{p}(\mathbf{v}, \Omega) = \mathbf{0}, \tag{17}$$

where $\mathbf{p}$ is a $P_N(2m+1) \times 1$ non-linear vector function of $\mathbf{v}$ and Ω. For given $\mathbf{v}$ and rotational speed Ω (and hence $\varpi = \Omega/N$), $\mathbf{p}(\mathbf{v}, \Omega)$ can be computed. This enables a solution of equation (17) for $\mathbf{v}$ to be obtained by iteration. The only receptance terms in $\mathbf{S}$ that need computation are those linking the non-linear degrees of freedom with the non-zero elements in $\mathbf{f}$. Since the unbalance forces/moments are harmonic at single frequency Ω, the only elements in the Fourier coefficient vectors $\bar{\mathbf{f}}$, $\mathbf{f}_C^s$, $\mathbf{f}_S^s$ that need computation by Fourier analysis at each stage of the iteration are the Fourier coefficients of the squeeze film forces. For given $\mathbf{v}$, the time histories of these forces are established by computation of the non-linear expressions of equation (2) at a suitable number of points over one period $\Gamma = 2\pi/\varpi$. Fourier analyses of these time histories are then performed. Equation (17) is solved using a predictor–corrector iterative procedure. The Newton–Raphson iterative method is used as the corrector with initial approximations provided by a linear polynomial (predictor), to trace out a speed response curve of periodic solutions. Use of the rotational speed Ω as the control parameter to advance the solution procedure along the speed response curve results in failure when more than one solution $\mathbf{v}$ is possible for a given rotational speed Ω (as in bistable regions). Arc-length continuation is used to overcome this problem [12]. The control parameter is changed from Ω to an "arc-length" σ. The rotational speed Ω becomes an unknown, $\Omega = \Omega(\sigma)$ and an extra equation needs to be added to system (17). Suppose that $\mathbf{v}$ and Ω are required for $\sigma = \sigma_i$ i.e., $\mathbf{v}_i$, Ω_i are required. Suppose that $\mathbf{v}_{i-1}$, Ω_{i-1}, corresponding to $\sigma = \sigma_{i-1}$ are known. The extra equation to be added defines σ in the interval $\sigma_{i-1} \leqslant \sigma \leqslant \sigma_i$:

$$g(\mathbf{v}, \Omega, \sigma) = \frac{1}{c^2} \| \mathbf{v} - \mathbf{v}_{i-1} \| + \left(\frac{\Omega}{\omega_0} - \frac{\Omega_{i-1}}{\omega_0} \right)^2 - (\sigma - \sigma_{i-1})^2 = 0, \tag{18}$$

where for a vector $\mathbf{a} = [a_1 \cdots a_n]^{\mathrm{T}}$, $\| \mathbf{a} \| = a_1^2 + \cdots + a_n^2$. c is the radial clearance of any one of the dampers and ω_0 is the lowest natural frequency of the undamped linear system. Note that c and ω_0 are merely introduced in order to work with a non-dimensional arc-length σ. The system of equations to be solved for each given value of σ, σ_i, is

$$\left\{ \begin{matrix} \mathbf{p}(\mathbf{v}, \Omega) = \mathbf{0} \\ g(\mathbf{v}, \Omega, \sigma) = 0 \end{matrix} \right\}. \tag{19}$$

The vector of unknowns is now augmented to

$$\mathbf{v}_{aug} = \begin{bmatrix} \mathbf{v} \\ \Omega \end{bmatrix}. \tag{20}$$

The solution procedure "climbs" along the speed response curve, so that a given value of σ will correspond to just one solution $\mathbf{v}_{aug}$, thus eliminating the problem of multiple solutions. In order to start off the continuation process at $\sigma = 0$, the initial approximation for $\mathbf{v}$ is provided by the Fourier coefficients of a time marching solution, when assumed approximations are unsuccessful.

Upon solution of equation (17) for $\mathbf{v}$ over a range of values of Ω and determination of the associated values of $\bar{\mathbf{f}}$, $\mathbf{f}_C^s$, $\mathbf{f}_S^s$, the response in any of the remaining P_L degrees of freedom can be found from equations (16). The only receptance terms in $\mathbf{T}$ that need computation are those linking the chosen degree of freedom with the non-zero elements in $\mathbf{f}$.

In equations (15a, 16a), it has been implicitly assumed that all zero frequency terms in $\mathbf{S}_0$, $\mathbf{T}_0$ exist. This condition holds when the rotor in the *remnant linear subsystem* is supported at not less than two positions. When this is not the case, the rotor is said to be degenerate and is capable of free rigid body motion, so that some or all of the terms in $\mathbf{S}_0$ and $\mathbf{T}_0$ will be undefined ($\rightarrow \infty$). In such a case, equations (15a) and (16a) are modified as follows.

The static load of the rotor is included in $\mathbf{f}$, concentrated at one or more of the degrees of freedom in the y direction.

$\mathbf{h}_0$ is omitted and the displacements in $\mathbf{h}$ are measured from the static positions of the bearing housings without the rotor load acting. Similarly, the displacements $\mathbf{g}$ at the remaining degrees of freedom are measured from the static condition without the rotor weight applied.

In equation (15a), those k rows in $\mathbf{S}_0$ for which the receptances are undefined are replaced by the corresponding rows in the zero frequency value $\mathbf{A}_0$ of the accelerance matrix $\mathbf{A}$ where

$$\mathbf{A} = -\omega^2 \mathbf{S}. \tag{21}$$

The terms in $\mathbf{A}_0$ will be defined. The corresponding k terms on the left-hand side of (15a) will be replaced by the corresponding zero frequency (mean) acceleration terms in the Fourier expansion of $\ddot{\mathbf{u}}$, and hence will all be zero (by differentiation of equation (12a) twice).

The resulting modified k equations, in equations (15a) are a statement of the fact that the degenerate rotor will be in equilibrium under those elements in the zero frequency force vector $\bar{\mathbf{f}}$ that act on it. These equations are solved along with the remaining $P_N(2m+1)-k$ equations in equations (15) as previously described. Only a maximum of 4 of these zero frequency equilibrium equations can be independent. When $k>4$, a statically indeterminate equilibrium problem at zero frequency needs to be solved within equations (15). A typical case is a rotor that is supported by squeeze film dampers only, without retainer springs, where the number of dampers $n_{SFD}\geqslant 3$. Such a case is not considered in this paper.

2.3. DIFFERENTIAL EQUATIONS OF MOTION

The RHB method works exclusively in the frequency domain. However, in order to test the stability of the equilibrium solutions computed by RHB (and of course, for time marching purposes), the time domain differential equations of motion of the non-linear system are required. A modal approach is adopted to derive these equations. In this analysis, in contrast to RHB, the vector $\mathbf{f}_N$ comprises *all* the damping forces, linear, as well as non-linear and any gyroscopic moments (if significant). By considering all these forces/moments as external, it is possible to work with the modal parameters (i.e., natural frequencies and mode shapes) of the undamped non-rotating remnant subsystem, which will be real and independent of rotational speed. The modal parameters can be obtained by using any convenient linear modelling technique. As shall be illustrated later, receptance functions can be used to determine both the modal parameters and the number of modes required. In practice, only a limited number of modes H, will make a significant contribution to the response and hence

$$\mathbf{u}\approx\mathbf{Hq}, \tag{22}$$

where $\mathbf{q}$ is the $(H\times 1)$ vector of modal co-ordinates

$$\mathbf{q}=[q_1\ \cdots\ q_H]^{\mathrm{T}}, \tag{23}$$

and $\mathbf{H}$ is the $(P\times H)$ modal matrix

$$\mathbf{H}=[\Psi^1\ \cdots\ \Psi^H], \tag{24}$$

where Ψ^h, $h=1\cdots H$ are the mass normalized mode shapes [13]. The corresponding natural frequencies are contained in the diagonal matrix $\mathbf{D}$, given by

$$\mathbf{D}=\mathrm{diag}\,(\omega_1^2\ \cdots\ \omega_H^2). \tag{25}$$

The modal equations are hence given [5] by

$$\ddot{\mathbf{q}}+\mathbf{Dq}=\mathbf{H}^{\mathrm{T}}\mathbf{f}\,(\mathbf{u}_N,\dot{\mathbf{u}}_N,t), \tag{26}$$

where $\mathbf{f}(\mathbf{u}_N,\dot{\mathbf{u}}_N,t)$ is given by equation (6). By partitioning $\mathbf{H}$ as follows

$$\mathbf{H}=\begin{bmatrix}\mathbf{H}_N\\ \mathbf{H}_L\end{bmatrix}, \tag{27}$$

where $\mathbf{H}_N$ and $\mathbf{H}_L$ are of dimension $(P_N \times H)$ and $(P_L \times H)$, respectively, $\mathbf{u}_N$ in equation (7) can be expressed as

$$\mathbf{u}_N = \mathbf{H}_N \mathbf{q}. \tag{28}$$

2.4. FLOQUET STABILITY OF EQUILIBRIUM SOLUTIONS AND BIFURCATION

The stability of an RHB-computed equilibrium periodic solution $\mathbf{u}_E$ of fundamental frequency ϖ is tested by considering the evolution of a small perturbation from it. Defining $\tau = \varpi t$ and $(\ )'$ as differentiation with respect to τ, the modal equations (26) are rewritten as

$$\mathbf{q}'' + \frac{1}{\varpi^2}\mathbf{D}\mathbf{q} = \frac{1}{\varpi^2}\mathbf{H}^{\mathrm{T}}\left\{\begin{bmatrix}\mathbf{f}_N(\mathbf{u}_N, \mathbf{u}'_N)\\ \mathbf{0}\end{bmatrix} + \mathbf{f}_R(\tau)\right\}, \tag{29}$$

where equation (6) has been used to substitute for $\mathbf{f}(\mathbf{u}_N, \mathbf{u}'_N, \tau)$. Now, from equation (28)

$$\mathbf{u}_E = \mathbf{H}\mathbf{q}_E. \tag{30}$$

$\mathbf{u}_E(\tau)$ is periodic in τ with period 2π and so is $\mathbf{q}_E(\tau)$, which satisfies equation (29),

$$\mathbf{q}''_E + \frac{1}{\varpi^2}\mathbf{D}\mathbf{q}_E = \frac{1}{\varpi^2}\mathbf{H}^{\mathrm{T}}\left\{\begin{bmatrix}\mathbf{f}_{NE}(\mathbf{u}_{NE}, \mathbf{u}'_{NE})\\ \mathbf{0}\end{bmatrix} + \mathbf{f}_R(\tau)\right\}, \tag{31}$$

where from equation (28):

$$\mathbf{u}_{NE} = \mathbf{H}_N \mathbf{q}_E. \tag{32}$$

Upon defining

$$\mathbf{z} = \mathbf{q} - \mathbf{q}_E \tag{33}$$

and subtracting equation (31) from equation (29),

$$\mathbf{z}'' + \frac{1}{\varpi^2}\mathbf{D}\mathbf{z} = \frac{1}{\varpi^2}\left[\mathbf{H}_N^{\mathrm{T}}\ \mathbf{H}_L^{\mathrm{T}}\right]\begin{bmatrix}\dfrac{\partial \mathbf{f}_N}{\partial \mathbf{u}_N}(\mathbf{u}_N - \mathbf{u}_{NE}) + \dfrac{\partial \mathbf{f}_N}{\partial \mathbf{u}'_N}(\mathbf{u}'_N - \mathbf{u}'_{NE})\\ \mathbf{0}\end{bmatrix}, \tag{34}$$

where equation (27) has been used to substitute for $\mathbf{H}$ and $\mathbf{f}_N(\mathbf{u}_N, \mathbf{u}'_N)$ has been expanded in a Taylor series about $\mathbf{u}_{NE}$, $\mathbf{u}'_{NE}$ and only linear terms in $(\mathbf{u}_N - \mathbf{u}_{NE})$ and $(\mathbf{u}'_N - \mathbf{u}'_{NE})$ retained. Upon noting from equations (28), (32) and (33) that $\mathbf{u}_N - \mathbf{u}_{NE} = \mathbf{H}_N\mathbf{z}$, equation (34) becomes

$$\mathbf{z}'' + \frac{1}{\varpi^2}\mathbf{D}\mathbf{z} = \frac{1}{\varpi^2}\mathbf{H}_N^{\mathrm{T}}\frac{\partial \mathbf{f}_N}{\partial \mathbf{u}_N}\mathbf{H}_N\mathbf{z} + \frac{1}{\varpi^2}\mathbf{H}_N^{\mathrm{T}}\frac{\partial \mathbf{f}_N}{\partial \mathbf{u}'_N}\mathbf{H}_N\mathbf{z}'. \tag{35}$$

Upon letting

$$\mathbf{w} = \begin{bmatrix}\mathbf{z}\\ \mathbf{z}'\end{bmatrix}, \tag{36}$$

equation (35) can be written in the form

$$\mathbf{w}' = \mathbf{W}(\tau)\,\mathbf{w}, \tag{37}$$

where

$$\mathbf{W}(\tau) = \begin{bmatrix} \mathbf{0} & \mathbf{I}_H \\ \mathbf{U}(\tau) - \dfrac{1}{\varpi^2}\mathbf{D} & \mathbf{V}(\tau) \end{bmatrix} \tag{38}$$

$$\mathbf{U}(\tau) = \frac{1}{\varpi^2}\,\mathbf{H}_N^{\mathrm{T}}\,\frac{\partial \mathbf{f}_N}{\partial \mathbf{u}_N}\,\mathbf{H}_N, \quad \mathbf{V}(\tau) = \frac{1}{\varpi^2}\,\mathbf{H}_N^{\mathrm{T}}\,\frac{\partial \mathbf{f}_N}{\partial \mathbf{u}'_N}\,\mathbf{H}_N. \tag{39a, b}$$

Since the partial derivatives in the $(H \times H)$ matices $\mathbf{U}(\tau)$ and $\mathbf{V}(\tau)$ are evaluated at the equilibrium conditions $\mathbf{u}_N = \mathbf{u}_{NE}$, $\mathbf{u}_N = \mathbf{u}'_{NE}$, they are periodic in τ with period 2π and hence so is the $(2H \times 2H)$ matrix $\mathbf{W}(\tau)$. From Floquet Theory, the stability of equation (37) is governed by the eigenvalues of the *monodromy* matrix $\mathbf{M}$ [12, 14]. This matrix is efficiently computed by an approximate method by Hsu [15]. The periodic interval $[0, 2\pi]$ is divided into K equal segments $\Delta\tau$ with τ_k, $k = 1 \cdots K$, the value of τ at the midpoint of each segment. $\mathbf{M}$ is then approximated as

$$\mathbf{M} \approx \mathrm{e}^{\mathbf{W}_K \Delta\tau}\,\mathrm{e}^{\mathbf{W}_{K-1}\Delta\tau} \cdots \mathrm{e}^{\mathbf{W}_2 \Delta\tau}\,\mathrm{e}^{\mathbf{W}_1 \Delta\tau}, \tag{40}$$

where

$$\mathbf{W}_k = \mathbf{W}(\tau_k). \tag{41}$$

The above matrix product converges to the exact matrix $\mathbf{M}$ as $K \to \infty$. However, in the simulations performed in this paper, $K = 200$ gave highly accurate results with little computational effort. For $\mathbf{u}_E$ stable,

$$|\lambda_i| < 1,\ i = 1 \cdots 2H: \tag{42}$$

i.e., the eigenvalues of $\mathbf{M}$ (also known as Floquet multipliers) lie within a unit circle in the complex plane centred at the origin. If, as a control parameter (e.g., rotational speed) is changed, the leading eigenvalue λ_l (eigenvalue of largest magnitude) escapes from the circle, then $\mathbf{u}_E$ becomes unstable (i.e., a bifurcation occurs) [12]. If λ_l escapes the unit circle along the positive real axis, then any disturbance from $\mathbf{u}_E$ results in a jump to a periodic attractor of the same period. If λ_l escapes the unit circle along the negative real axes then a period-doubling bifurcation occurs. If a pair of complex conjugate eigenvalues λ_l, λ_l^* escape the circle, then a secondary Hopf bifurcation (quasi-periodicity) occurs. Note that, for an unstable solution $\mathbf{u}_E$, the position of the corresponding λ_l on the complex plane is not a definite indicator of the type of attractor on which the disturbed trajectory will settle down since Floquet Theory applies for *small* perturbations about $\mathbf{u}_E$. The attractor is positively identified by time marching from unstable equilibrium initial conditions.

In reference [1], $\mathbf{M}$ was computed from its text-book definition [12, 14]. Such a method is far too slow to test for the stability of a full set of equilibrium periodic solutions. In reference [2], Hsu's fast method was used, as in the present work. However, since Floquet Theory was applied to the FE equations rather than the modal equations, the order of the matrices in the exponents of the matrix product in equation (40) was $(2P \times 2P)$, making it impractical for large order systems. With the present method, the matrices in the exponents are cut down in size to $(2H \times 2H)$ where $H \ll P$.

2.5. TIME MARCHING

For time marching purposes, the system of equations (26) is expressed as $2H$ first order differential equations

$$\begin{bmatrix} \dot{\mathbf{q}} \\ \ddot{\mathbf{q}} \end{bmatrix} = \begin{bmatrix} \mathbf{0} & \mathbf{I}_H \\ -\mathbf{D} & \mathbf{0} \end{bmatrix} \begin{bmatrix} \mathbf{q} \\ \dot{\mathbf{q}} \end{bmatrix} + \begin{bmatrix} \mathbf{0} \\ \mathbf{H}^{\mathrm{T}}\ \mathbf{f} \end{bmatrix} \tag{43}$$

and integrated numerically from given initial conditions $\mathbf{q}(t=0)$, $\dot{\mathbf{q}}(t=0)$ by using an integrator suitable for stiff differential equations [16].

The result of the Floquet stability test for an equilibrium solution $\mathbf{u}_E$ can be confirmed by time marching from equilibrium initial conditions $\mathbf{q}_E\,(t=0)$, $\dot{\mathbf{q}}_E\,(t=0)$. If $\mathbf{u}_E$ is unstable, the slightest inevitable errors in the initial conditions and the local integration error in each time step cause the time marching trajectory to diverge from the equilibrium one. On the other hand, for $\mathbf{u}_E$ stable, both trajectories remain closely matched. This method serves to identify positively the attractor on which the disturbed trajectory will settle down, in the case of $\mathbf{u}_E$ being unstable. The initial conditions $\mathbf{q}_E\,(t=0)$, $\dot{\mathbf{q}}_E(t=0)$ are found by a modal decomposition of the RHB solution $\mathbf{u}_E$ as follows. The RHB responses at H degrees of freedom, arbitrarily chosen, are computed. These are contained in the vector $\mathbf{u}_{HE}$. The corresponding velocity vector $\dot{\mathbf{u}}_{HE}$ is then formed (by differentiation of equation (12a)). From equation (30)

$$\mathbf{q}_E(t=0) = \mathbf{H}_H^{-1}\,\mathbf{u}_{HE}\,(t=0), \quad \dot{\mathbf{q}}_E(t=0) = \mathbf{H}_H^{-1}\,\dot{\mathbf{u}}_{HE}\,(t=0), \tag{44a, b}$$

where the matrix $\mathbf{H}_H$ $(H \times H)$ comprises H rows of $\mathbf{H}$, respectively corresponding to the chosen H degrees of freedom in $\mathbf{u}_{HE}$.

2.6. INTEGRATED NON-LINEAR MODELLING APPROACH

The integrated non-linear modelling approach presented in this paper is summarized in Figure 3. The operating conditions (unbalance, static misalignments at the dampers) are first specified. A speed response curve of approximate $N=1$ equilibrium periodic solutions (see equation (11)) is then traced out by using RHB with a suitable number of harmonics m. The resulting RHB solution set is then tested for stability by using the Floquet test. Any unstable branches of the speed response curve are then classified according to the position of λ_l on the complex plane. An unstable equilibrium cycle along one such branch is then considered. Time marching from initial conditions on the cycle locates an attractor. If the resulting attractor is NT-periodic, where T is the period of rotation ($=2\pi/\Omega$), then the branch is reanalyzed by using RHB with the appropriate value for N. If the attractor is aperiodic then the whole branch has to be reanalyzed by time marching. Frequency spectra (modulus of Fast Fourier Transform (FFT)) and Poincare maps are used to analyze the time marching solution. Poincare maps show a stroboscopic picture of the x–y vibration trajectory (orbit) at a given location at intervals of T i.e., the "return points" $x(kT)$, $y(kT)$, $k=0, 1, \ldots$. Hence, NT-periodic motion would appear as N distinct points on the map.

3. APPLICATION

3.1. DESCRIPTION OF TEST RIG

The model is applied to the experimental rig illustrated in Figure 4. The mild steel stepped shaft runs in self-aligning ball-bearings at H and J. The one at H is rigidly

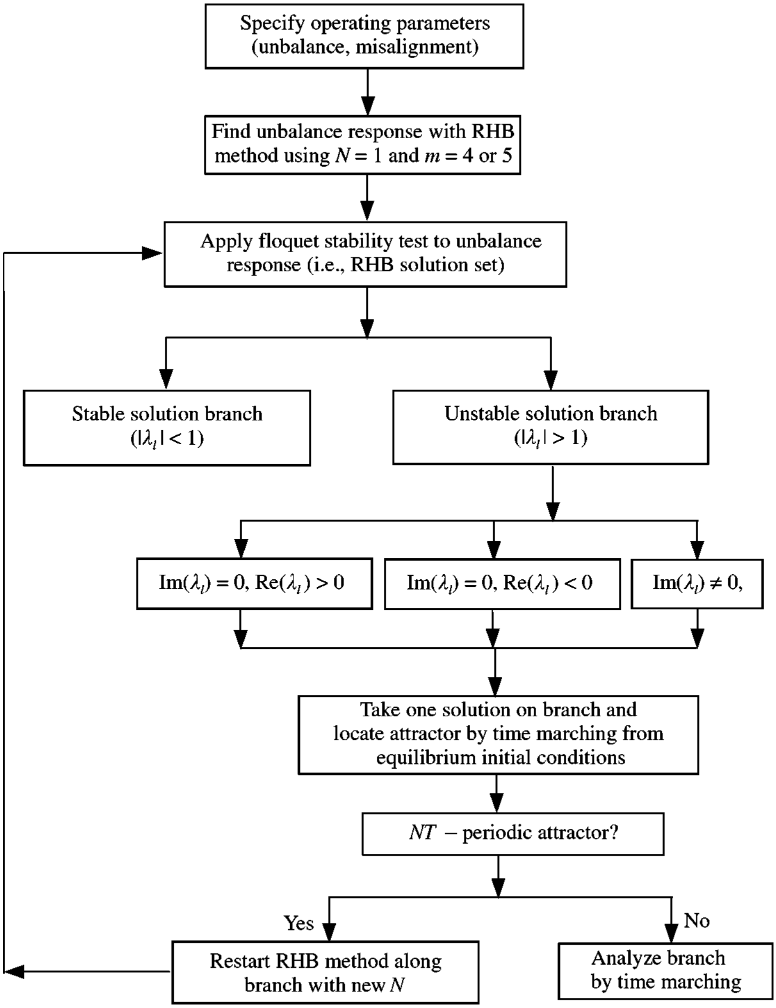

Figure 3. Flow chart for integrated non-linear analysis process (RHB = receptance harmonic balance).

supported while that at J is free to orbit in an oil-filled annular clearance in the bearing housing B, forming the SFD. Two configurations (i, ii) of the rig are considered. In the first configuration (i), four flexible bars (labelled (5) in Figure 4) connect the outer race of the ball-bearing at J (i.e., the journal) to the frame, constituting an isotropic retainer spring of stiffness 123·4 kN/m. If the frame is taken to be rigid and B is rigidly bolted to the frame, the spring is effectively in parallel with the squeeze film. However, since the spring is grounded at F rather than B, the static eccentricity of the journal J in the bearing housing B can be varied by altering the position of B. In configuration (ii) the retainer spring is removed and the journal J rests on the bottom of the clearance in the static condition. In this case, an anti-rotation bolt is used to prevent the journal from rotating with the shaft. The SFD is of the type shown in Figure 1(b). Its parameters are: radial clearance $c = 0{\cdot}132$ mm, bearing bore $R = 50{\cdot}022$ mm, land length $L = 9{\cdot}72$ mm. Oil of viscosity $\eta = 0{\cdot}0045\,\mathrm{Ns/m^2}$ is supplied through three holes, equally spaced along the groove. With reference again to Figure 4, unbalance masses are attached to the overhung disc at U. The x and y vibrations

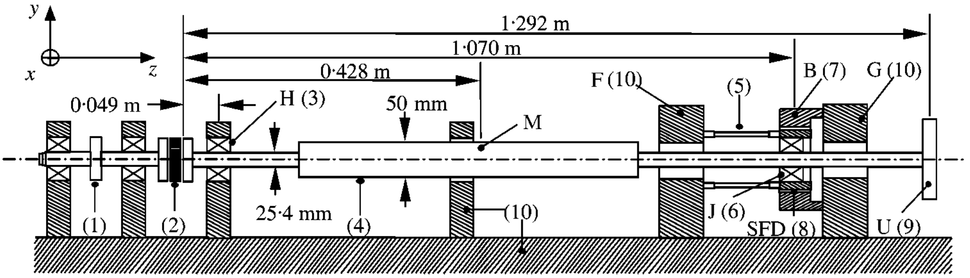

Figure 4. Test rig used for experimental validation of simulations: (1) motor driven pulley; (2) flexible coupling; (3) self-aligning ball-bearing (H); (4) flexible shaft; (5) flexible bar × 4 (retainer spring); (6) self-aligning ball-bearing (J); (7) bearing housing (B); (8) squeeze film damper (SFD); (9) overhung unbalance disc (U); (10) frame and bedplate.

are monitored at three positions J, U, and M. M is the midpoint of the 50 mm diameter section of the shaft. Safety regulations limit the maximum operational speed to 100 rev/s. All results presented refer to an unbalance of $U = 5{\cdot}1 \times 10^{-4}$ kg m at U. In configuration (i) (retainer spring in place), the static misalignments ε_{0xJ} ($= e_{0xJ}/c$), ε_{oyJ} ($= e_{oyJ}/c$) of J in the x and y directions are, respectively, equal to 0·0, − 0·8.

3.2. MODEL APPLICATION

3.2.1. *Introduction*

The mechanical impedance (MI) method [7] is used to compute the receptances of the remnant linear subsystem. The frame, bearing housing B and self-aligning ball-bearings at H and J are taken to be rigid; hence the remnant subsystem will be the shaft pinned at H and either sprung or unsprung (free) at J (i.e., configurations (i), (ii) respectively). The moments of inertia of the disc and shaft are neglected, and therefore, so are any gyroscopic effects. Hence, in the remnant subsystem, the xz and yz planes are uncoupled. The SFD is assumed to be the only source of damping. The detailed input to the MI modelling program is given in reference [17]. The shaft elements, modelled as Timoshenko beams, are continuous with respect to inertia and the impedance matrix of a uniform element is "exact", irrespective of element length [7]. Hence, in this application, only eight elements are necessary. The first two undamped critical speeds of configuration (i) are found to be 14 and 40 rev/s by MI. In the interpretation of both experimental and simulated results, it is important to know the undamped critical speeds of the rig with the SFD clearance shimmed solid (i.e, damper "locked": shaft pinned at H and J). These speeds are found to be 31 and 91 rev/s by MI.

In the non-linear modelling, for both the RHB and modal equations, $P_N = 2$ and

$$\mathbf{f}_N = \begin{bmatrix} Q_x(X_J, Y_J, \dot{X}_J, \dot{Y}_J) \\ Q_y(X_J, Y_J, \dot{X}_J, \dot{Y}_J) \end{bmatrix}, \qquad (45)$$

where Q_x, Q_y are the squeeze film forces on J (equation 2)) and X_J, Y_J are the displacements of J measured from the centreline of the rigid bearing housing B. The unbalance forces P_x, P_y at U are given by putting $\phi_k = 0$ in equation (1) and dropping the subscript k.

3.2.2. *Configuration* (*i*) (*retainer spring in place*)

In this case

$$\mathbf{u}_N = \begin{bmatrix} X_J \\ Y_J \end{bmatrix} - \begin{bmatrix} e_{0xJ} \\ e_{0yJ} \end{bmatrix}. \tag{46}$$

In the RHB approach

$$X_J = \bar{X}_J + \sum_{s=1}^{m} (a^s_{XJ} \cos s\varpi t + b^s_{XJ} \sin s\varpi t), \quad Y_J = \bar{Y}_J + \sum_{s=1}^{m} (a^s_{YJ} \cos s\varpi t + b^s_{YJ} \sin s\varpi t), \tag{47a, b}$$

and

$$Q_x = \bar{Q}_x + \sum_{s=1}^{m} (p^s_x \cos s\varpi t + q^s_x \sin s\varpi t), \quad Q_y = \bar{Q}_y + \sum_{s=1}^{m} (p^s_y \cos s\varpi t + q^s_y \sin s\varpi t), \tag{48a, b}$$

where the Fourier coefficients of the squeeze film forces are given by

$$\bar{Q}_x = \frac{1}{\Gamma}\int_0^{\Gamma} Q_x \, \mathrm{d}t, \quad p^s_x = \frac{2}{\Gamma}\int_0^{\Gamma} Q_x \cos s\varpi t \, \mathrm{d}t, q^s_x = \frac{2}{\Gamma}\int_0^{\Gamma} Q_x \sin s\varpi t \, \mathrm{d}t, \tag{49a}$$

$$\bar{Q}_y = \frac{1}{\Gamma}\int_0^{\Gamma} Q_y \, \mathrm{d}t, \quad p^s_y = \frac{2}{\Gamma}\int_0^{\Gamma} Q_y \cos s\varpi t \, \mathrm{d}t, q^s_y = \frac{2}{\Gamma}\int_0^{\Gamma} Q_y \sin s\varpi t \, \mathrm{d}t. \tag{49b}$$

Hence, the RHB equations (15) are writting as:

$$\bar{X}_J - e_{0xJ} = \bar{Q}_x \alpha_{JJ}(0), \qquad \bar{Y}_J - e_{0yJ} = \bar{Q}_y \beta_{JJ}(0), \tag{50a1, a2}$$

$$a^s_{XJ} = \alpha_{JJ}(s\varpi)\, p^s_x, \qquad a^s_{YJ} = \beta_{JJ}(s\varpi)\, p^s_y - \delta_{Ns}\beta_{JU}(s\varpi)\, U\Omega^2, \quad s = 1 \cdots m. \tag{50b1, b2}$$

$$b^s_{XJ} = \alpha_{JJ}(s\varpi)\, q^s_x + \delta_{Ns}\alpha_{JU}(s\varpi)\, U\Omega^2, \quad b^s_{YJ} = \beta_{JJ}(s\varpi)\, q^s_y, \quad s = 1 \cdots m, \tag{50c1, c2}$$

where

$$\delta_{Ns} = \begin{Bmatrix} 0 & s \neq N \\ 1 & s = N \end{Bmatrix}; \tag{51}$$

(see equation (11)) and $\alpha_{ij}(\omega)$ and $\beta_{ij}(\omega)$ are the receptances connecting the forces (in N) at *position j* in the x and y directions, respectively, with the responses (in m) in the corresponding directions at position i. These receptances are real and independent of rotational speed as a result of the simplifying assumptions made. Also, since the remnant system is isotropic, $\alpha_{ij}(\omega) = \beta_{ij}(\omega)$. For solution, equations (50) are expressed in the form (17) where $\mathbf{v}$ is a $2(2m + 1) \times 1$ vector given by

$$\mathbf{v} = [\bar{X}_J \ \bar{Y}_J \ a^1_{XJ} \ a^1_{YJ} \ \cdots \ a^m_{XJ} \ a^m_{YJ} \ b^1_{XJ} \ b^1_{YJ} \ \cdots \ b^m_{XJ} \ b^m_{YJ}]^{\mathrm{T}}. \tag{52}$$

Upon solution and determination of the Fourier coefficients of Q_x, Q_y, the Fourier coefficients of the dynamic response at a general position P:

$$X_P = \bar{X}_P + \sum_{s=1}^{m} (a^s_{XP} \cos s\varpi t + b^s_{XP} \sin s\varpi t), \quad Y_P = \bar{Y}_P + \sum_{s=1}^{m} (a^s_{YP} \cos s\varpi t + b^s_{YP} \sin s\varpi t), \tag{53a, b}$$

are determined from equations (50) by omitting the terms e_{0xJ}, e_{0yJ}, replacing the subscript J by P in the displacement Fourier coefficients on the left-hand sides of equations (50) and replacing the *first* subscript J by P in the receptance terms on the right-hand sides of equations (50).

For the modal equations of motion, four modes of bending vibration in *each* of the xz and yz planes are considered so that $H = 8$ and the vector $\mathbf{q}$ (equation (23)) and matrix $\mathbf{D}$ (equation (25)) are written as

$$\mathbf{q} = [q_{x1} \;\; q_{y1} \;\; \cdots \;\; q_{x4} \;\; q_{y4}]^{\mathrm{T}}, \tag{54}$$

$$\mathbf{D} = \mathrm{diag}(\omega_{x1}^2 \;\; \omega_{y1}^2 \;\; \cdots \;\; \omega_{x4}^2 \;\; \omega_{y4}^2). \tag{55}$$

The modal equations hence reduce to

$$\ddot{q}_{xr} + \omega_{xr}^2 q_{xr} = \psi_{xJ}^r Q_x(X_J, Y_J, \dot{X}_J, \dot{Y}_J) + \psi_{xU}^r P_x(t), \quad r = 1 \cdots 4, \tag{56a}$$

$$\ddot{q}_{yr} + \omega_{yr}^2 q_{yr} = \psi_{yJ}^r Q_y(X_J, Y_J, \dot{X}_J, \dot{Y}_J) + \psi_{yU}^r P_y(t), \quad r = 1 \cdots 4, \tag{56b}$$

where ψ_{xi}^r, ψ_{yi}^r, $r = 1 \cdots 4$, are the undamped mass normalized mode shapes at position i in the x and y directions respectively. Note that $\omega_{xr} = \omega_{yr}$ and $\psi_{xi}^r = \psi_{yi}^r$ (isotropic system). In equations (56), from equation (28):

$$\begin{bmatrix} X_J \\ Y_J \end{bmatrix} = \begin{bmatrix} e_{0xJ} \\ e_{0yJ} \end{bmatrix} + \mathbf{H}_N \mathbf{q}, \tag{57}$$

where

$$\mathbf{H}_N\,(2 \times 8) = \begin{bmatrix} \psi_{xJ}^1 & 0 & \cdots & \psi_{xJ}^4 & 0 \\ 0 & \psi_{yJ}^1 & \cdots & 0 & \psi_{yJ}^4 \end{bmatrix}. \tag{58}$$

The undamped natural frequencies $\omega_{x1} \cdots \omega_{x4}$ are found by locating the first four zeros of the determinant of the impedance matrix $\{z_{ij}(\omega)\}$, given by

$$\{z_{ij}(\omega)\} = \{\alpha_{ij}(\omega)\}^{-1}/\mathrm{j}\omega, \tag{59}$$

upon using Muller's algorithm [18]. As the natural frequencies are known, the required mode shapes are found by decomposing the receptances $\alpha_{ij}(\omega)$ over four modes by using an approximate truncated modal series expansion for $\alpha_{ij}(\omega)$ [13],

$$\alpha_{ij}(\omega) \approx \sum_{r=1}^{4} \frac{A_{ij}^r}{\omega_{xr}^2 - \omega^2}, \tag{60}$$

where A_{ij}^r, $r = 1 \cdots 4$, are the modal constants, given by [13]

$$A_{ij}^r = \psi_{xi}^r \psi_{xj}^r. \tag{61}$$

The computed modal parameters are given in Table 1. Figures 5(a, b) compare the "exact" receptances $\alpha_{JJ}(\omega)$, $\alpha_{JU}(\omega)$, computed by MI, with the approximate receptances, reconstructed from four modes (i.e, the right-hand side of equation (60)). It is evident that satisfactory agreement prevails over a frequency range of 0–500 Hz, covering five harmonics of the top rotational speed of the rig (100 rev/s).

TABLE 1

Undamped modal parameters of configuration (i) *in one plane of vibration*

Mode no. r	$f_{xr} = \omega_{xr}/(2\pi)$ (Hz)	$A^r_{JJ} = \psi^r_{xJ}\psi^r_{xJ}$ ($\times 10^{-3}$ kg^{-1})	$A^r_{JU} = \psi^r_{xJ}\psi^r_{xU}$ ($\times 10^{-3}$ kg^{-1})
1	13·7	54·235	77·803
2	40·4	38·334	− 34·209
3	173·9	251·196	− 38·783
4	334·7	104·839	− 13·606

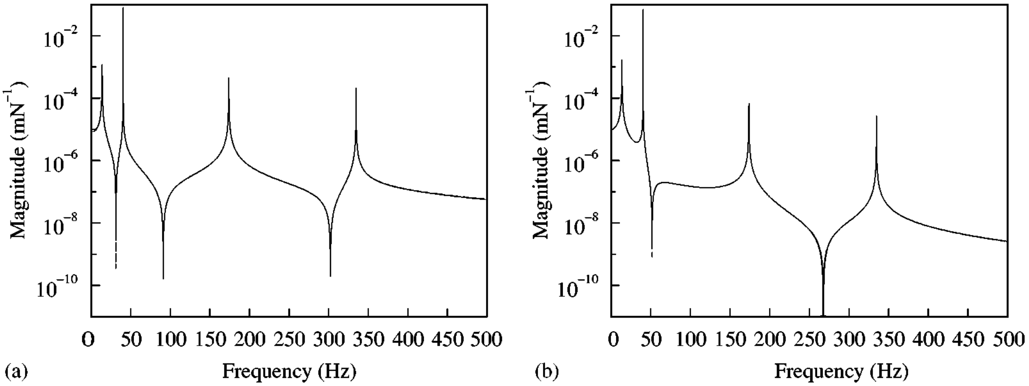

Figure 5. Receptances for configuration (i) (retainer spring in place). (a) Point receptance at J, α_{JJ}, (b) Transfer receptance between J and U, α_{JU}: ——, exact (MI); - - -, reconstructed from four modes.

For stability and bifurcation analysis, the matrices $\partial \mathbf{f}_N/\partial \mathbf{u}_N$, $\partial \mathbf{f}_N/\partial \mathbf{u}'_N$ in (39a, b) are given by

$$\frac{\partial \mathbf{f}_N}{\partial \mathbf{u}_N} = \begin{bmatrix} \dfrac{\partial Q_x}{\partial X_J} & \dfrac{\partial Q_x}{\partial Y_J} \\ \dfrac{\partial Q_y}{\partial X_J} & \dfrac{\partial Q_y}{\partial Y_J} \end{bmatrix}, \quad \frac{\partial \mathbf{f}_N}{\partial \mathbf{u}'_N} = \begin{bmatrix} \dfrac{\partial Q_x}{\partial X'_J} & \dfrac{\partial Q_x}{\partial Y'_J} \\ \dfrac{\partial Q_y}{\partial X'_J} & \dfrac{\partial Q_y}{\partial Y'_J} \end{bmatrix}. \tag{62a, b}$$

The partial derivatives in these matrices are evaluated numerically at the RHB-computed periodic equilibrium solution from the expressions for Q_x and Q_y given in equation (2).

3.2.3. *Configuration* (*ii*) (*no retainer spring*)

In this case, the rotor in the remnant linear subsystem is degenerate since it is capable of free rigid body rotation about H, so that $\alpha_{ij}(0)$ is undefined at all positions i along the rotor (except the node H). It is assumed that the distributed gravity load can be replaced by a concentrated load at J equal to W, the equivalent static load at the squeeze film, given by

$$W = \frac{\sum M_x}{l_J}, \tag{63}$$

TABLE 2

Undamped modal parameters of configuration (ii) *in one plane of vibration*

Mode no. r	$f_{xr} = \omega_{xr}/(2\pi)$ (Hz)	$A^r_{JJ} = \psi^r_{xJ}\psi^r_{xJ}$ ($\times 10^{-3}$ kg^{-1})	$A^r_{JU} = \psi^r_{xJ}\psi^r_{xU}$ ($\times 10^{-3}$ kg^{-1})
1	0	66·771	81·309
2	39·0	31·507	– 36·914
3	171·6	248·118	– 39·777
4	334·2	102·339	– 13·415

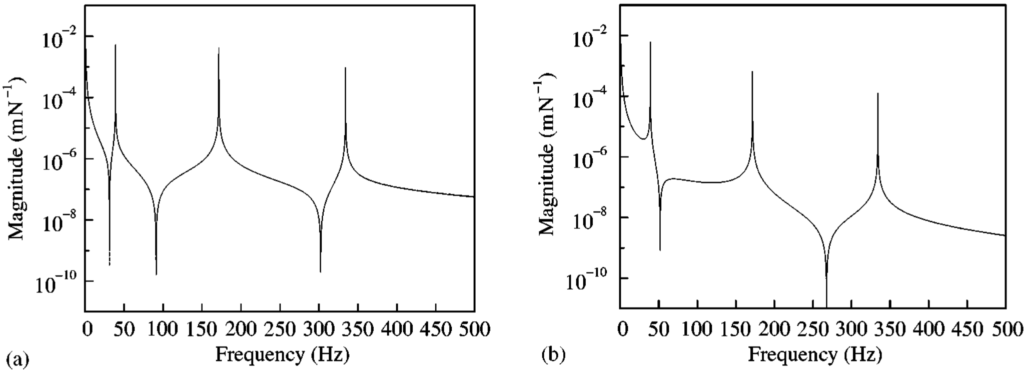

Figure 6. Receptances for configuration (ii) (no retainer spring)· (a) Point receptance at J, α_{JJ}, (b) Transfer receptance between J and U, α_{JU}: ——, exact (MI); – – –, reconstructed from 4 modes.

where $\sum M_x$ is the sum of clockwise moments of gravity forces about H and l_J the distance of SFD from pivot H. W is computed as 151 N. Accordingly, the equations in section 3.2.2 are modified as follows.

The vector $[e_{0xJ} \;\; e_{0yJ}]^{\mathrm{T}}$ is omitted.

The zero frequency RHB equations (50a1, a2) are replaced by the following equilibrium equations (obtained by taking moments about H):

$$\bar{Q}_x = 0, \quad \bar{Q}_y - W = 0. \tag{64a, b}$$

The zero frequency Fourier coefficients $\bar{X}_P$, $\bar{Y}_P$ in equations (53a, b) are given by

$$\bar{X}_P = \frac{l_J}{l_P}\bar{X}_J, \quad \bar{Y}_P = \frac{l_J}{l_P}\bar{Y}_J, \tag{65a, b}$$

where l_P is the distance of P from pivot H. The reason for this is that the only zero frequency forces acting on the rotor are concentrated at J, producing no deformation. X_P, Y_P are now measured from the line joining H to the centreline of B.

An additional term $-\psi^r_{yJ}W$ is added to equations (56b) to account for the static load.

As for configuration (i), the modal equations cover four modes in each of the xz and yz planes. The computed modal parameters are shown in Table 2, where it is seen that the first mode for each plane is the rigid body mode (0 Hz). Figures 6(a, b) compare the "exact"

TABLE 3

Static eccentricity adjustment for $\varepsilon_{0xJ} = 0{\cdot}0$, $\varepsilon_{0yJ} = -0{\cdot}8$ (*configuration* (i))

θ (°)	ε_{0xJ}	θ (°)	ε_{0yJ}
(a1) x direction, 25°C		(a2) y direction, 25°C	
0	– 0·03	0	– 0·63
90	0·03	90	– 0·84
180	– 0·03	180	– 0·96
270	– 0·07	270	– 0·77
$\bar{\varepsilon}_{0xJ}$	– 0·03	$\bar{\varepsilon}_{0yJ}$	– 0·80
(b1) x direction, 33°C		(b2) y direction, 33°C	
0	0·02	0	– 0·66
90	0·05	90	– 0·91
180	0·07	180	– 1·00
270	– 0·05	270	– 0·86
$\bar{\varepsilon}_{0xJ}$	0·02	$\bar{\varepsilon}_{0yJ}$	– 0·86

receptances $\alpha_{JJ}(\omega)$, $\alpha_{JU}(\omega)$, computed by MI with the approximate receptances, reconstructed from four modes. As in configuration (i), satisfactory agreement prevails over a frequency range of 0–500 Hz, covering five harmonics of the top rotational speed of the rig (100 rev/s).

3.3. EXPERIMENTAL WORK

For configuration (i) (retainer spring in place), the static eccentricities (misalignments) of the journal J from the bearing housing B were adjusted by loosening the screws bolting B to the frame at G (see Figure 4). A small clearance in the screw holes through B allowed its position to be adjusted prior to retightening. The adjustment of the eccentricity was complicated by the initial bend ("run-out") of the shaft, which meant that the static misalignment varied as the shaft was turned by hand. Hence, the eccentricity was adjusted in the vertical and horizontal directions for four angular positions (0, 90, 180, 270°) of the shaft (see Table 3). The angular position 0° corresponds to the "high spot" on the shaft at the SFD position. For each direction x, y the average eccentricity for the four angular positions was brought as close as possible to the desired eccentricity in that direction. The static misalignment was rechecked after each experiment, when the rig was hot (Table 3). For both configurations (i, ii) the x, y vibration data (time histories) were obtained by three pairs of orthogonal displacement transducers located at J, U and M for each speed in the range 10–100 rev/s, in incremental steps of 2 rev/s. The oil supply pressure was set to 1 bar in configuration (i) and 1.2 bar in configuration (ii). An eight channel *HP3566A*® *Analyzer* coupled with a personal computer was used to capture the time histories. For configuration (ii) only, the frequency analyzer only acquired the alternating component of the response. The time capture length was 0·5 s. Hence the resolution of the frequency spectrum was 2 Hz. This resolution was generally considered adequate since a 2 rev/s step was the smallest attainable with the speed controller. However, the data length was increased to 2 s at those speeds where a more detailed frequency spectrum was required. The data were converted to *MATLAB*® data format for analysis using standard data conversion program.

3.4. RESULTS AND DISCUSSION

3.4.1. *Introduction*

In this section, the simulated results are compared with measurements with the aim of illustrating the practical value of the integrated non-linear model. It is outside the scope of this paper to give a detailed interpretation of the experimental results. This can be found in reference [17], where the influence of cavitation within the squeeze film is discussed. Moreover, in the simulations, no attempt was made to compensate for the small residual out-of-balance on the shaft left after balancing. In all simulated and experimental results presented, the vibration response at all locations is normalized with respect to the radial clearance c. Moreover, the orbital motion at the SFD (J) is presented with respect to the clearance circle, of radius c, to which the motion of the centre of the journal, J, is confined. Orbital motions at locations U and M are presented with respect to their static positions.

3.4.2. *Configuration* (*i*) (*retainer spring in place*)

In Figures 7(a–f), the experimentally determined unbalance response (half peak-to-peak amplitude) in the x and y directions at the locations, J, U, M is compared with the corresponding RHB, $N = 1$ predictions with $m = 5$ harmonics. In Figures 7(a, b), which refer to the response at J, an anti-resonance speed of around 52 rev/s is evident. This corresponds to the anti-resonance in the transfer receptance α_{JU} (52 Hz) in Figure 5(b). The maximum amplitude at the three locations lies within the range 32–36 rev/s. It is seen that the vibration at all three locations is reasonably well predicted, with the exception of the disc vibration in the x direction in the range 26–36 rev/s (Figure 7(c)). A possible explanation for this is given by comparing the predicted and measured orbital motion in Figure 8, which refers to locations U and M at 28 and 38 rev/s. The motion at the disc (U) is characterized by an elliptical orbit. The orientation of this orbit changes as the resonance region is traversed. The mismatch in orientation between predicted and measured orbits at 28 rev/s, Figure 8(a1), results in a large discrepancy in the peak-to-peak amplitude in the x direction, but little discrepancy in the y direction. The predicted and measured disc orbits are realigned at 38 rev/s and beyond (Figure 8(a2)). The orbits at M below 38 rev/s are sharply kinked, as shown in Figure 8(b1), reflecting the strong presence of harmonics of the rotational speed. The kinked outline of the measured orbit in Figure 8(b1) is correctly predicted by RHB with $m = 5$ harmonics. These sharp kinks disappear at 38 rev/s and beyond (Figure 8(b2)). The corresponding orbits at the SFD (J) for 28 and 38 rev/s are shown in Figures 12(a) and 12(c) respectively. In particular, the sharpening of the left-hand "tail" of the SFD orbit at 38 rev/s is correctly predicted. Such pronounced tails should be avoided in practice, since the rapid decelerations and accelerations in the vicinity of the tail may lead to sudden large changes in the force transmitted to the engine frame [19].

The results of the Floquet stability test for the RHB, $N = 1$ predictions are shown in Figure 9. Instability is detected in the range 32–35 rev/s (Figure 9(a)), the magnitude of the leading Floquet multiplier being greater than unity and the multiplier complex (Figure 9(b)). This indicates that a secondary Hopf bifurcation occurs at around resonance, resulting in quasi-periodic motion in this region. This result is confirmed by time marching the modal equations from equilibrium initial conditions at two speeds, 30 and 34 rev/s, which are, respectively, outside and inside this instability range. In each case, initial conditions are derived from a modal decomposition of the RHB solution (equations (44a,b)). Figure 10 refers to 30 rev/s. The time marching solution covers the last 5 shaft

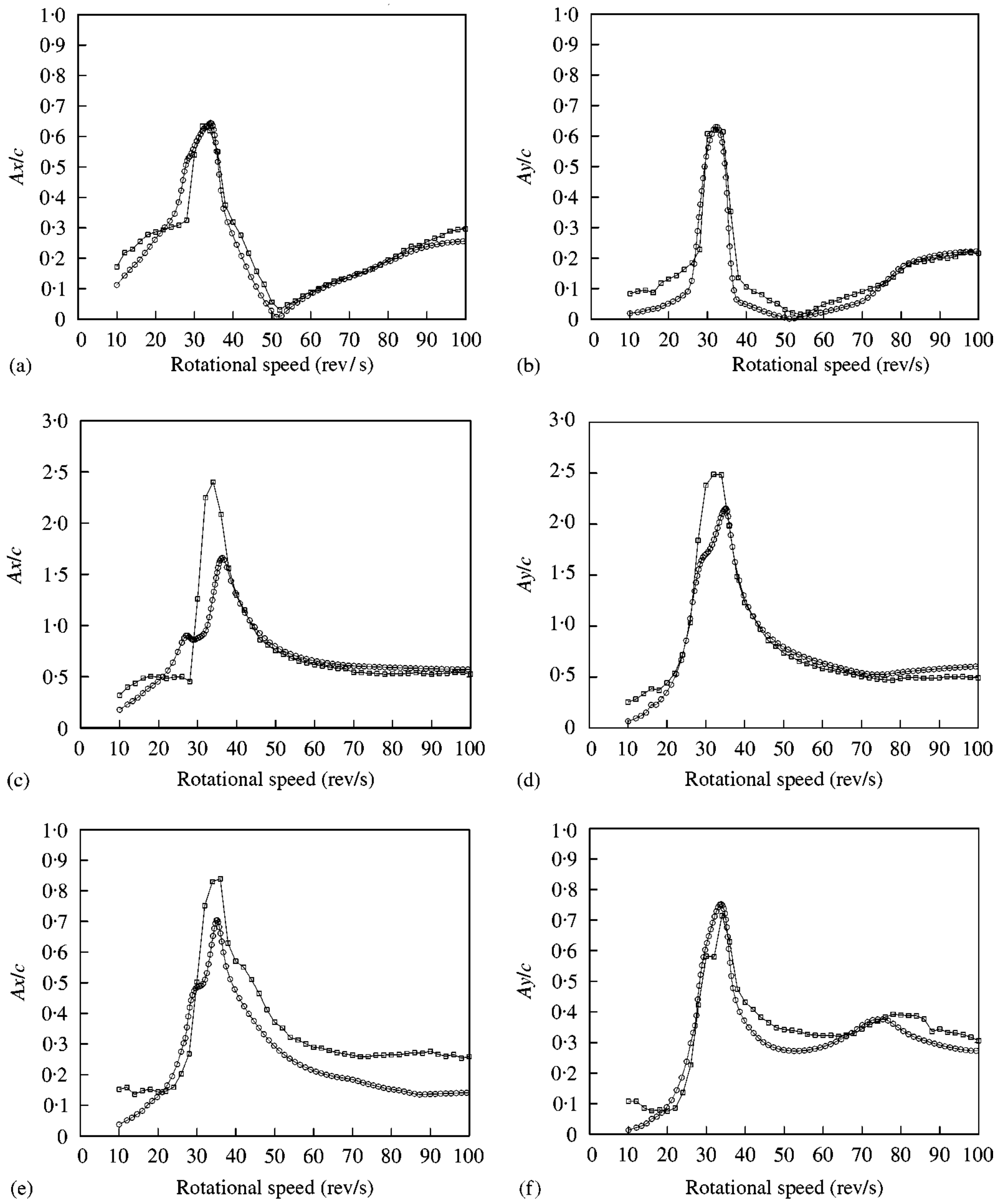

Figure 7. Unbalance response (normalized half peak to peak) for configuration (i), $\varepsilon_{0xJ} = 0$, $\varepsilon_{0yJ} = -0{\cdot}8$. (a) SFD (J), x direction; (b) SFD (J), y direction; (c) disc (U), x direction; (d) disc (U), y direction; (e) mid-shaft (M), x direction; (f) mid-shaft (M), y direction: —○—, Predictions, RHB, $N = 1$, $m = 5$; —□—, measurement.

revolutions out of a total of 15 revolutions. The RHB solution is overlaid on the same axes. It is seen that the trajectories remain closely matched, indicating that the RHB-computed $N = 1$ periodic cycle at 30 rev/s is indeed an attractor. Figure 10 also serves to highlight the excellent correlation that exists between the RHB and modal techniques at all three locations J, U, M. At 34 rev/s (Figure 11(a)), the time marching and RHB trajectories

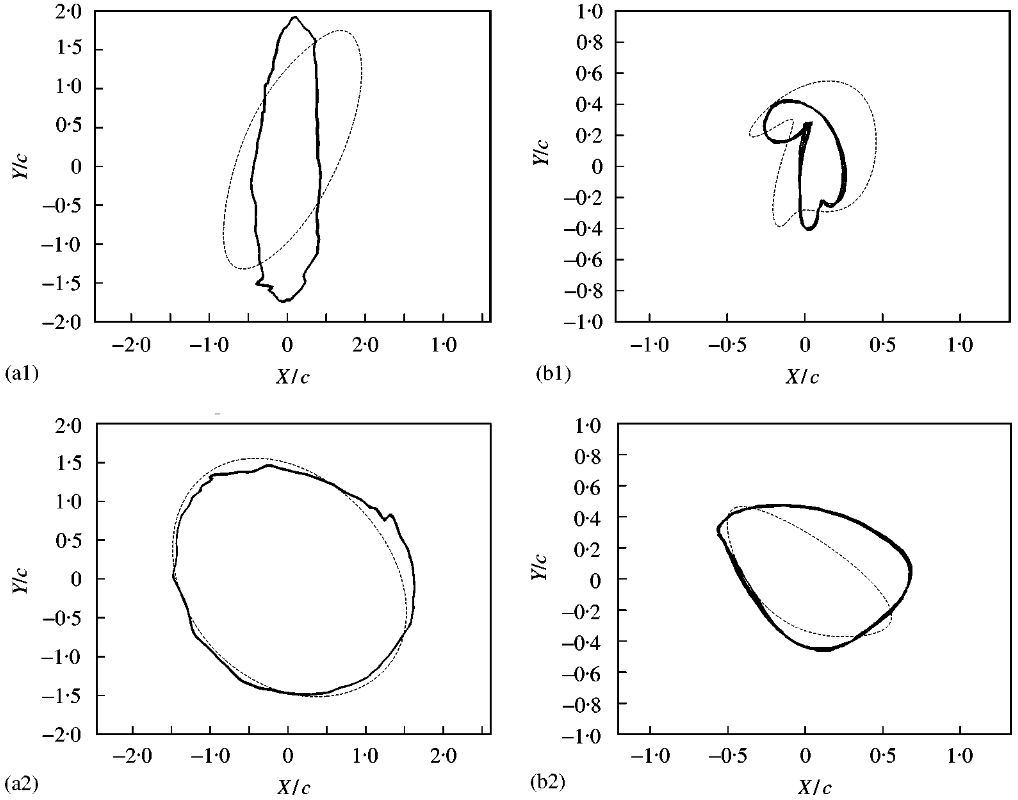

Figure 8. Orbital motion of U and M for configuration (i), $\varepsilon_{0xJ} = 0$, $\varepsilon_{0yJ} = -0{\cdot}8$. (a1) U (disc), 28 rev/s; (b1) M (mid-shaft), 28 rev/s; (a2) U (disc), 38 rev/s; (b2) M (mid-shaft), 38 rev/s: - - -, Prediction: RHB, $N = 1$, $m = 5$; ——, measurement (0·5 s).

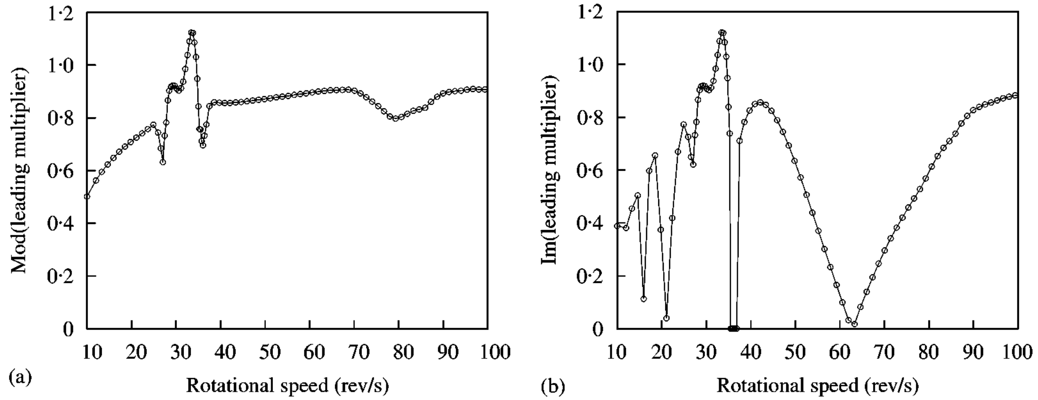

Figure 9. Floquet stability test for RHB solutions $N = 1$, $m = 5$, configuration (i) $\varepsilon_{0xJ} = 0$, $\varepsilon_{0yJ} = -0{\cdot}8$: (a) absolute value of leading multiplier; (b) imaginary part of leading multiplier.

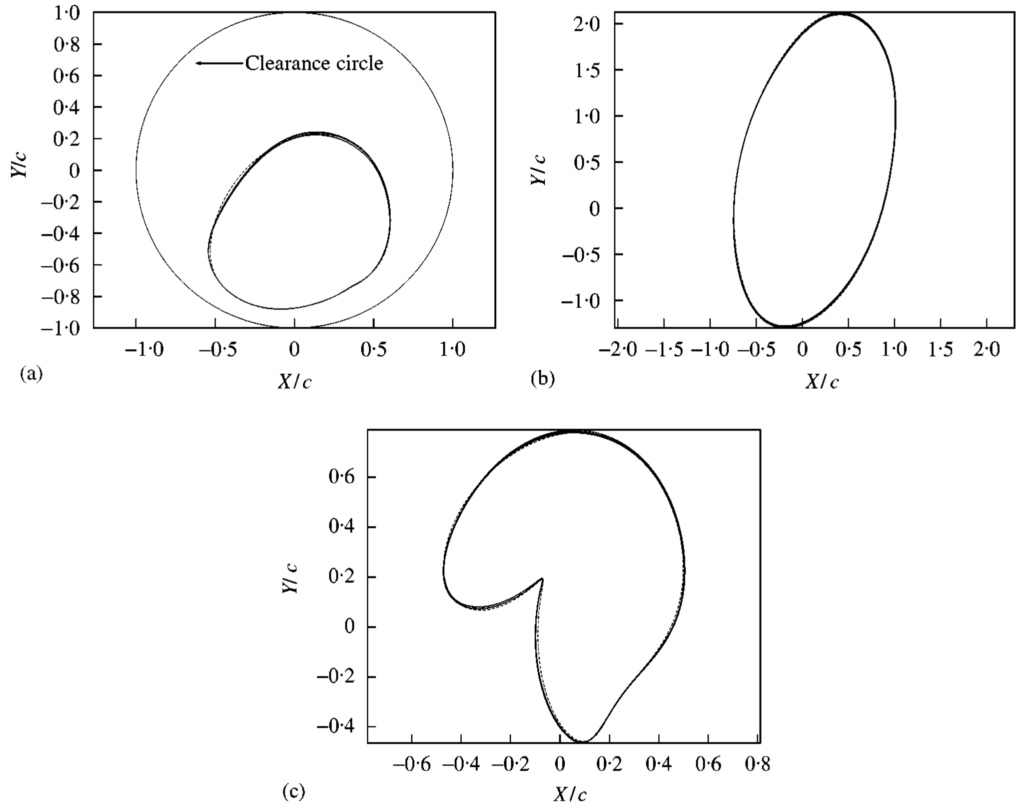

Figure 10. Stability check by time marching from equilibrium initial conditions: predicted orbits at 30 rev/s, configuration (i), $\varepsilon_{0xJ} = 0$, $\varepsilon_{0yJ} = -0{\cdot}8$. (a) J (SFD); (b) U (disc); (c) M (mid-shaft) - - -, RHB, $N = 1$, $m = 5$; ——, modal solution.

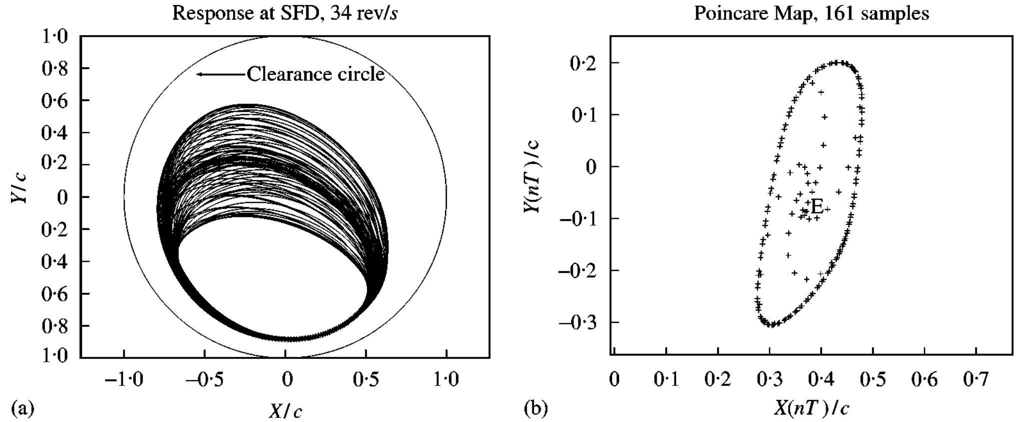

Figure 11. Stability check by time marching from equilibrium initial conditions at 34 rev/s, configuration (i), $\varepsilon_{oxJ} = 0$, $\varepsilon_{0yJ} = -0{\cdot}8$. (a) SFD orbit: ****, RHB, $N = 1$, $m = 5$; ——, modal solution (first 80 revs.), (b) Poincaré map over 160 shaft revs. (unstable equilibrium point is E, "*").

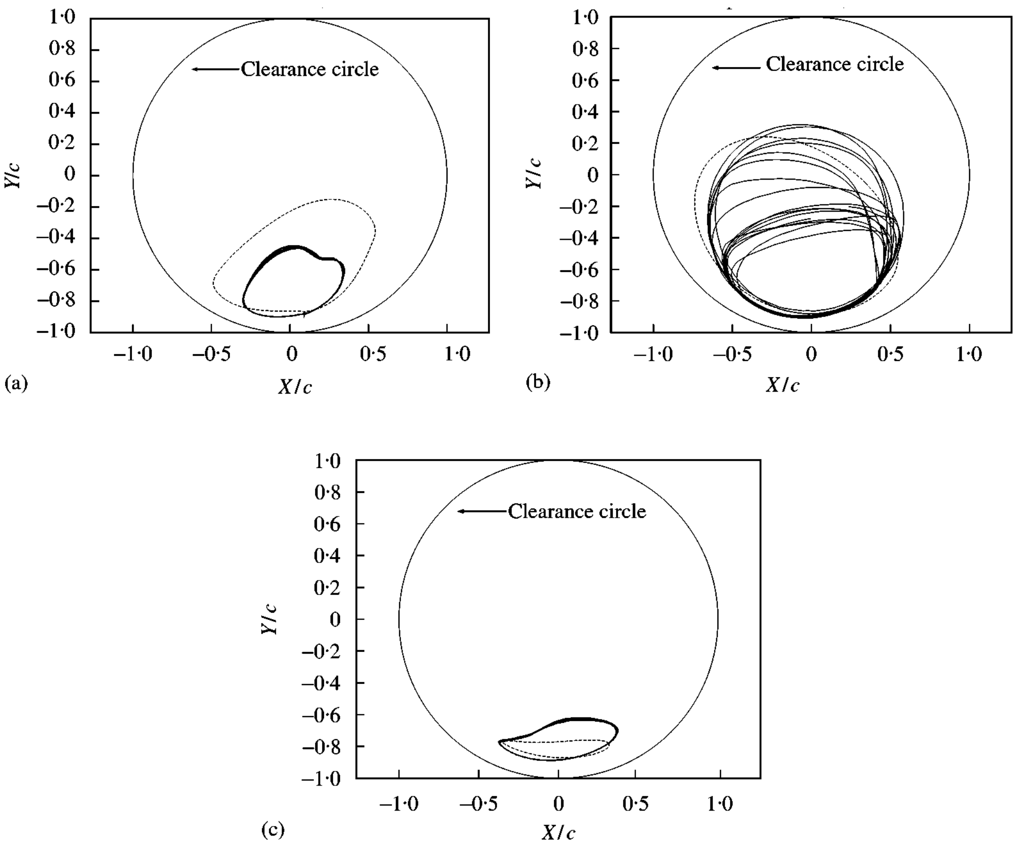

Figure 12. Orbital motion at SFD only for configuration (i), $\varepsilon_{0xJ} = 0$, $\varepsilon_{0yJ} = -0{\cdot}8$. (a) 28 rev/s; (b) 34 rev/s; (c) 38 rev/s: – – –, Prediction: RHB, $N = 1$, $m = 5$; ——, measurement (0·5 s).

diverge. The Poincaré Map (Figure 11(b)) shows the return points spiralling out of the initial unstable equilibrium point E and settling into a “drift ring” of points that never quite coincide. This is the hall mark of quasi-periodic motion and is the result of two irrationally related fundamental frequency components [12]. Aperiodic motion was also verified in practice, over a speed range of 30–36 rev/s, as shown in Figure 12(b). Figure 13 shows the predicted and measured steady state orbits at the SFD at 34 rev/s and their frequency spectra for the y vibration. The measurement acquisition time was increased to 2 s (frequency resolution 0·5 Hz). Both predicted and measured spectra exhibit sub-synchronous activity. The predicted spectrum (Figure 13(a2)) has a strong 9 Hz component and sum and difference frequency components are apparent e.g., 25 (= 34 − 9) Hz, 43 (= 34 + 9) Hz, 59 = (68 − 9) Hz. Sum and difference frequency components are characteristic of quasi-periodicity. The measurement (Figure 13(b2)) also contains the 9 Hz component, along with some other components not predicted, such as 13 Hz and 21 (= 34 − 13) Hz. The fuzzy continuity in the measured spectrum is an indication of chaos. It is possible that the quasi-periodic attractor was disturbed due to the variation of the static misalignment with rotation due to the initial bend in the shaft (Table 3).

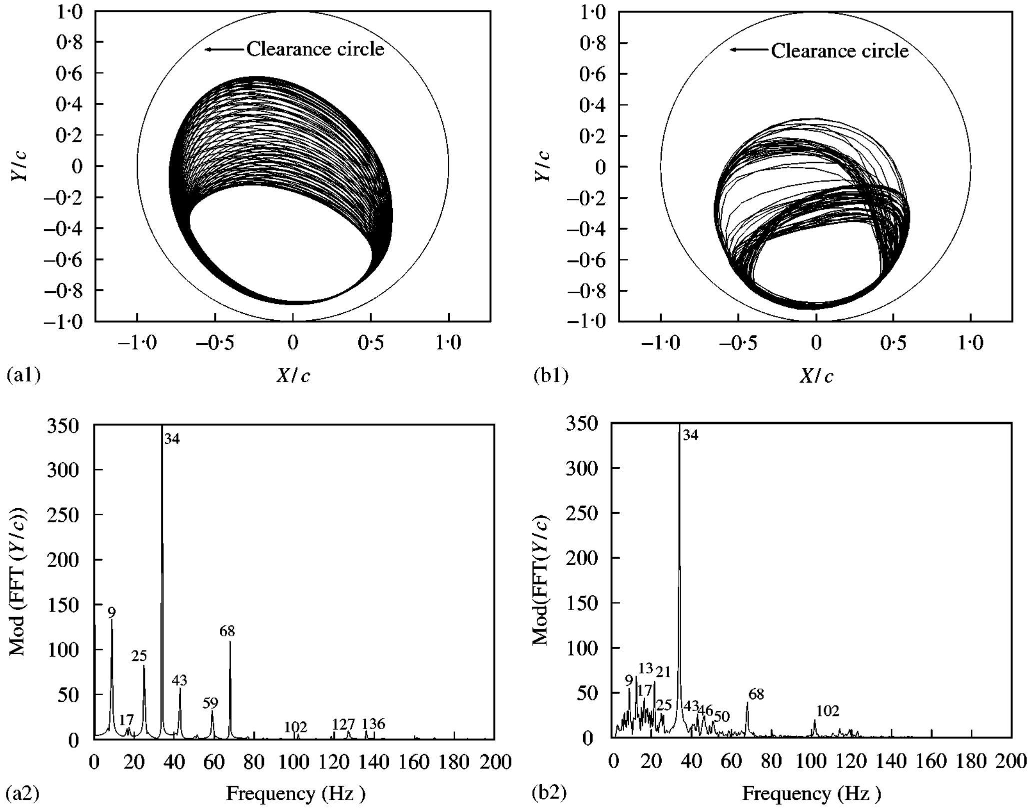

Figure 13. SFD orbits and spectra at 34 rev/s for configuration (i), $\varepsilon_{0xJ} = 0$, $\varepsilon_{0yJ} = -0{\cdot}8$. (a1) predicted SFD orbit (steady state); (b1) measured SFD orbit (2 s); (a2) predicted spectrum, y direction; (b2) measured spectrum, y direction.

3.4.3. *Configuration* (*ii*) (*no retainer spring*)

In Figures 14(a–f) the experimentally determined unbalance response (half peak-to-peak amplitude) in the x and y directions at the locations J, U, M is compared with the corresponding RHB, $N = 1$ predictions with $m = 5$ harmonics. The following observations can be made.

(1) At the SFD, in the y direction especially, there is hardly any vibration except in the regions around 31 and 90 rev/s. These correspond to the first two undamped critical speeds of the pinned–pinned shaft (31, 91 rev/s). The recorded values for half peak-to-peak amplitude at the SFD in the y direction around the first two critical speed regions and in the x direction, around the first, are actually greater than the radial clearance. This was probably due to the anti-rotation bolt acting on the outer race of J not functioning effectively, since the displacement probes at J were aimed at targets projecting from the outer race of J.

(2) Around the first critical speed (31 rev/s) the predicted speed response curve at all locations is very complicated, with multiple solutions.

(3) Except for location M in the y direction (Figure 14(f)), the vibration beyond 80 rev/s is under-predicted by the RHB $N = 1$ method, at all other locations, especially at the SFD. The disc vibrations (Figures 14(c, d)) are generally reasonably well predicted.

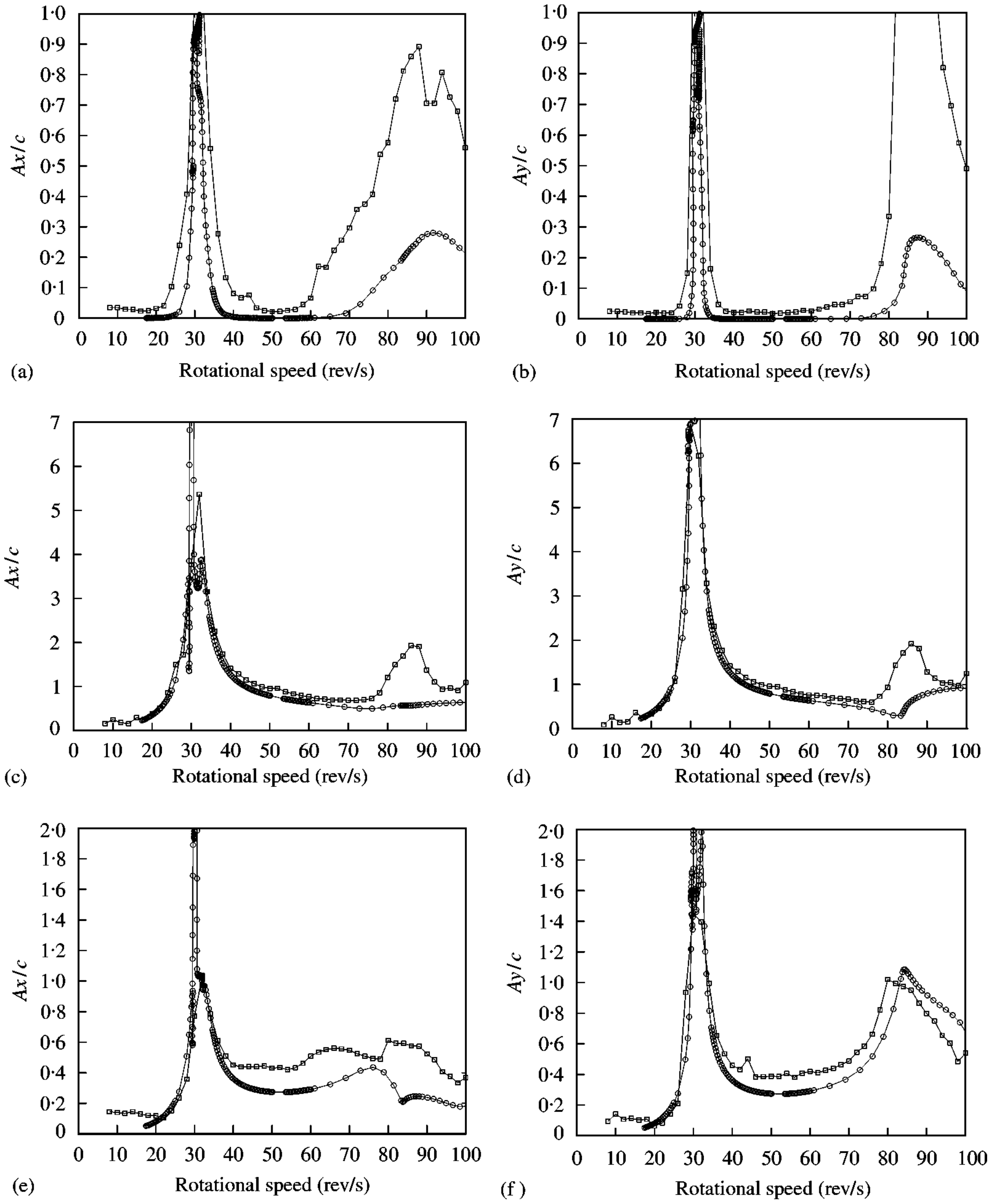

Figure 14. Unbalance response (normalized half peak to peak) for configuration (ii) (a) SFD (J), x direction; (b) SFD (J), y direction; (c) Disc (U), x direction; (d) Disc (U), y direction; (e) Mid-shaft (M), x direction; (f) Mid-shaft (M), y direction: —○—, Predictions, RHB, $N = 1$, $m = 5$; —□—, measurement.

The results of the Floquet stability test are shown in Figure 15. As can be seen, the RHB solutions outside the critical speed regions are on the threshold of stability. Around the first critical speed (30–31 rev/s) a multiplicity of solutions exists, some of which are stable, some unstable. Beyond 82 rev/s, all the RHB computed $N = 1$ solutions are clearly unstable. This helps to explain observation (3) above.

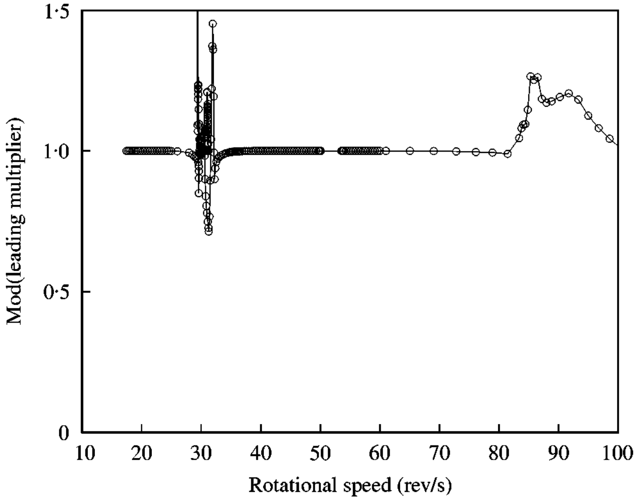

Figure 15. Floquet stability test for RHB solutions $N = 1$, $m = 5$, configuration (ii): absolute value of leading multiplier.

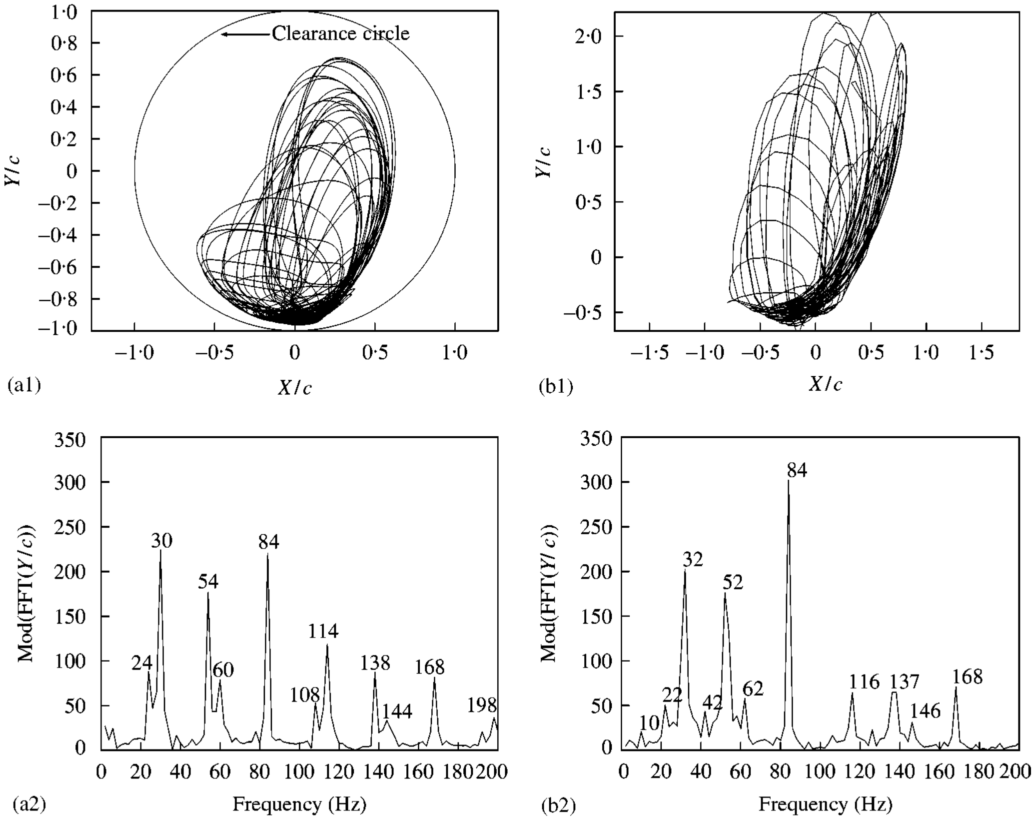

Figure 16. SFD orbit and spectra at 84 rev/s for configuration (ii). (a1) predicted SFD orbit (steady state); (b1) measured SFD orbit (0·5 s) — "a.c." only; (a2) predicted spectrum, y direction; (b2) measured spectrum, y direction.

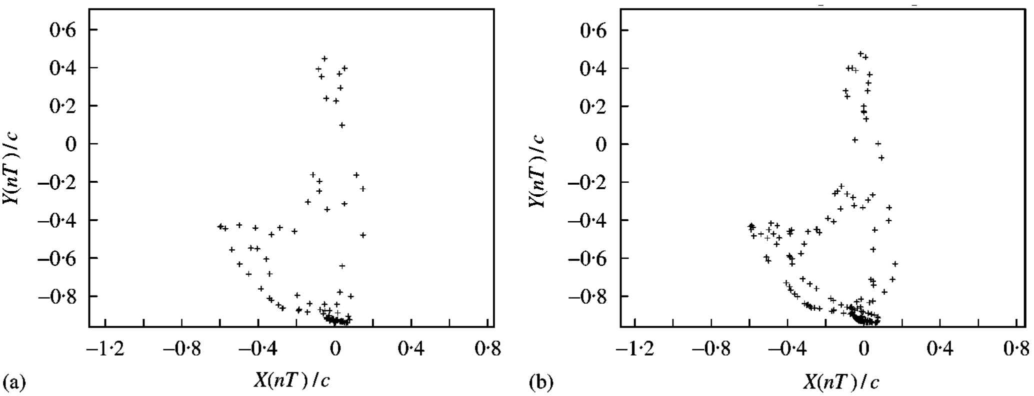

Figure 17. Poincaré maps for predicted SFD motion in Figure 16(a1). (a) 80 revolutions; (b) further 160 revolutions.

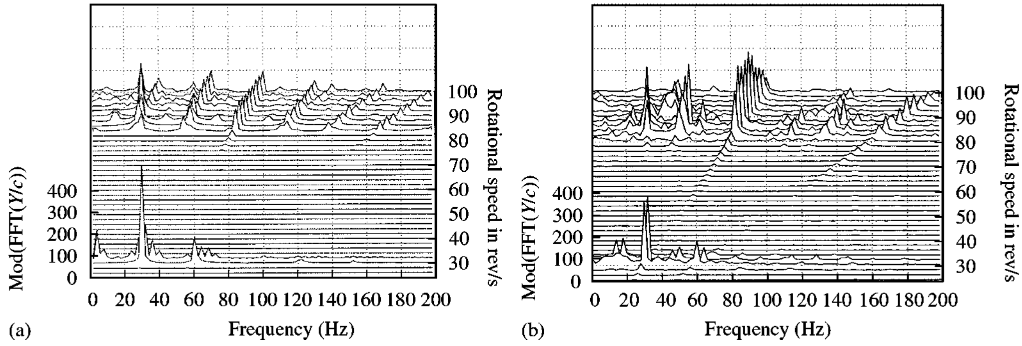

Figure 18. Waterfall diagrams of y vibration at J (SFD) for configuration (ii). (a) y direction, predicted; (b) y direction, measured.

Configuration (ii) was reanalyzed with the aim of constructing waterfall diagrams, showing the frequency spectrum of the response at different speeds. This was done by integrating the modal equations over 120 revolutions for each speed in the range 24–100 rev/s in incremental steps of 2 rev/s, using the final conditions of the previous speed as initial conditions for the next speed. Only the last 0·5 s of each response was analyzed. This was generally adequate to eliminate transients. Figure 16 compares the *steady state* modal solution at the SFD for 84 rev/s Figure 16(a1), with the measurement, Figure 16(b1). As mentioned earlier, in this configuration, the frequency analyzer only acquired the "alternating" component of the vibration. However, the measured orbit still bears a striking resemblance to the predicted orbit. Both orbits consist of two sets of opposing loops with a concentration of trajectories at the lower right-hand part of the orbit. Figures 16(a2, b2) show the corresponding frequency spectra for the y vibration. The frequency resolution is 2 Hz. Strong sub-synchronous components that loosely approximate to one-third and two-thirds sub-harmonic components appear in both measurement (32, 52 Hz respectively) and prediction (30, 54 Hz respectively), Additional minor sub-synchronous components are also evident in both measurement (22, 62 Hz) and prediction (24, 60 Hz). It is seen that most of the non-synchronous components are reasonably well predicted. The steady state predicted motion in Figure 16(a1) was examined with Poincaré maps. Figure 17(a) shows the Poincaré map over 80 shaft revolutions while Figure 17(b) shows a further 160 revolutions. It is seen that the general shape of the map is repeatable and that the return points seem to exhibit the fractal quality of a strange (chaotic) attractor [12]. The third-order sub-harmonic activity is prevalent in the region of the second pin–pin critical speed as shown in both predicted and measured waterfall diagrams for the y response: see Figure 18. The sub-harmonic resonance in this region is caused by the rotational speed being close to the three times the first pin–pin critical speed (31 rev/s).

4. CONCLUSIONS

In this paper, an efficient integrated technique for the non-linear modelling of unbalanced squeeze film damped rotor dynamic systems is developed. A receptance harmonic balance (RHB) technique is proposed for the determination of the steady state periodic response. This method is versatile and tractable for large order systems. The stability of the periodic response is tested by applying Floquet Theory to the modal equations of the system. The stability technique developed is more practical for large order systems than current methods in use. The results of the stability test can be confirmed by time marching the modal equations from equilibrium initial conditions obtained from a modal decomposition of the RHB solution. Time marching is also used to analyze aperiodic motion. The integrated technique is applied to a squeeze film damped rotor-bearing system in two configurations. Excellent correlation between the RHB solutions and modal analysis is achieved. Correlation with experimental results is also satisfactory. For the case studied, it is correctly predicted that for a highly eccentric damper with retainer spring, around the first pin–pin critical speed, the rotor is prone to aperiodic motion with sub-synchronous frequency components. The predicted aperiodic motion is of the quasi-periodic type. In the case of the unsupported squeeze film, the model successfully predicts strong third order sub-harmonic activity when the rotational speed is close to three times the first pin–pin critical speed.

While the technique presented has been developed for squeeze film damper applications, it is clear that it can be adapted to rotor dynamic systems with other types of non-linear elements by using the appropriate forcing functions in the vector $\mathbf{f}_N$, equation (6), instead of the expressions in equations (2a, b).

ACKNOWLEDGMENTS

The authors would like to acknowledge Mr Marc Burghardt for his contribution to the experimental work on configuration (ii) of the test rig.

REFERENCES

1. E. J. HAHN and P. Y. P. CHEN 1994 *American Society of Mechanical Engineers Journal of Tribology* **116**, 499–507. Harmonic balance analysis of general squeeze film damped multidegree-of-freedom rotor bearing systems.
2. J. Y. ZHAO, I. W. LINNETT and L. J. MCLEAN 1994 *American Society of Mechanical Engineers Journal of Tribology* **116**, 361–368. Stability and bifurcation of unbalanced response of a squeeze film damped flexible rotor.
3. T.-N. SHIAU and A.-N. JEAN 1990 *American Society of Mechanical Engineers Journal of Vibration and Acoustics* **112**, 501–507. Prediction of periodic response of Flexible mechanical systems with non-linear characteristics.

4. C. Nataraj and H. D. Nelson 1989 *American Society of Mechanical Engineers Journal of Vibration, Acoustics, Stress, and Reliability in Design* **111**, 187–193. Periodic solutions in rotor dynamic systems with nonlinear supports: a general approach.
5. R. W. Armentrout and E. J. Gunter 1999 *SPIE Proceedings* **3727**, 290–296. Transient modal analysis of nonlinear rotor-bearing systems.
6. J. Y. Zhao and E. J. Hahn 1993 *Proceedings of the Institution of Mechanical Engineers* **207**, 383–392. Subharmonic, quasi-periodic and chaotic motions of a rigid rotor supported by an eccentric squeeze film damper.
7. P. Bonello and M. J. Brennan 2001 *Journal of Sound and Vibration* **239**, 445–466. Modelling the dynamic behaviour of a supercritical rotor on a flexible foundation using the mechanical impedance technique.
8. A. Liew, N. S. Feng and E. J. Hahn 1999 *Proceedings of American Society of Mechanical Engineers Design Engineering Technical Conference: 17th Biennial Conference on Mechanical Vibration and Noise, September* 12–15, *Las Vegas*, Paper No. DETC99/VIB-8263, 9pp. Application of transfer matrices to non-linear rotor-bearing systems.
9. E. Kramer 1993 *Dynamics of Rotors and Foundations* Berlin: Springer-Verlag.
10. M. M. Dede, M. Dogan and R. Holmes 1985 *American Society of Mechanical Engineers Journal of Tribology* **107**, 411–418. The damping capacity of a sealed squeeze film bearing.
11. N. S. Feng and E. J. Hahn 1987 *American Society of Mechanical Engineers Journal of Tribology* **109**, 149–154. Effects of gas entrainment on squeeze film damper performance.
12. R. Seydel 1988 *From Equilibrium to Chaos: Practical Bifurcation and Stability Analysis.* Amsterdam: Elsevier Science.
13. D. J. Ewins 1984 *Modal Testing: Theory and Practice.* Letchworth: Research Student Press.
14. G. Ioos and D. D. Joseph 1980 *Elementary Stability and Bifurcation Theory.* Berlin: Springer-Verlag.
15. C. S. Hsu 1972 *American Society of Mechanical Engineers Journal of Applied Mechanics* **39**, 551–558. Impulsive parametric excitation: theory.
16. A. H. Craven and R. Holmes 1972 *International Journal for Numerical Methods in Engineering* **5**, 17–24. The vibration of engine crankshafts—a fast numerical solution.
17. P. Bonello, M. J. Brennan and R. Holmes 2000 *ISVR Technical Report No.* 292, *University of Southampton*, December 2000. A receptance based method for the non-linear modelling of squeeze film damped rotor dynamic systems.
18. S. D. Conte and C. De Boor 1972 *Elementary Numerical Analysis: An Algorithmic Approach.* New York: McGraw-Hill Book Company.
19. R. Holmes 1983 *American Society of Mechanical Engineers Journal of Engineering for Power* **105**, 525–529. The control of engine vibration using squeeze film dampers.

APPENDIX A: NOMENCLATURE

$a^s_{XJ}, a^s_{YJ}, a^s_{XP}, a^s_{YP}$	cosine coefficients in Fourier expansions of X_J, Y_J, X_P, Y_P respectively
A^r_{ij}	rth modal constant of receptance $\alpha_{ij}(\omega)$, equation (61) (kg^{-1})
$\mathbf{A}_0$	zero frequency value of accelerance matrix $\mathbf{A}$, equation (21)
$b^s_{XJ}, b^s_{YJ}, b^s_{XP}, b^s_{YP}$	sine coefficients in Fourier expansions of X_J, Y_J, X_P, Y_P respectively
c	radial clearance of damper (m)
$\mathbf{D}$	diagonal matrix of squares of natural frequencies, defined in equation (25)
e	eccentricity of J from B, Figure 1(a) (m)
e_{0xJ}, e_{0yJ}	static misalignments of J from B in x and y directions respectively (m)
$\mathbf{f}, \mathbf{f}_N, \mathbf{f}_L, \mathbf{f}_R$	force vectors defined in equation (6)
$\tilde{\mathbf{f}}$	complex amplitude of $\mathbf{f}$ for $\mathbf{f}$ harmonic
$\mathbf{f}_C, \mathbf{f}_S$	cosine and sine coefficient vectors of $\mathbf{f}$ for $\mathbf{f}$ harmonic, equation (9b)
$\bar{\mathbf{f}}, \mathbf{f}^s_C, \mathbf{f}^s_S$	Fourier coefficient vectors of $\mathbf{f}$, equation (12b)
$g(\mathbf{v}, \Omega, \sigma)$	arc-length function, equation (18)
$\mathbf{g}$	"linear" degrees of freedom vector, defined in equation (13b)
$\bar{\mathbf{g}}, \mathbf{g}^s_C, \mathbf{g}^s_S$	Fourier coefficient vectors of $\mathbf{g}$, as in equation (12a)
$\mathbf{h}$	vector of non-linear degrees of freedom at squeeze film dampers
$\mathbf{h}_0$	static value of $\mathbf{h}$
$\bar{\mathbf{h}}, \mathbf{h}^s_C, \mathbf{h}^s_S$	Fourier coefficient vectors of $\mathbf{h}$, as in equation (12a)

H	total number of modes considered in modal solution
$\mathbf{H}$, $\mathbf{H}_N$, $\mathbf{H}_L$	modal matrices defined in equations (24), (27)
$\mathbf{H}_H$	matrix comprising H rows of $\mathbf{H}$, equations (44a, b)
$\mathbf{I}_n$	$n \times n$ unit diagonal matrix i.e. with 1's on leading diagonal
K	total number of subdivisions for computation of $\mathbf{M}$, equation (40)
l_J, l_P	distances of J and P from ball-bearing H in Figure 4 (m)
L	land length (m)
m	total number of harmonics taken in receptance harmonic balance solution
$\mathbf{M}$	monodromy matrix, equation (40)
n_{SFD}, n_U	number of squeeze film dampers, unbalance discs respectively
N	$= \Omega/\varpi$, equation (11)
$p(\theta, z)$	instantaneous spatial pressure distribution in squeeze film (gauge, Pa)
p_c	cavitation pressure (gauge, Pa)
$p_m(\theta, z)$	modified pressure distribution, defined in equation (5) (gauge, Pa)
p_S	supply pressure (gauge, Pa)
p_x^s, p_y^x	cosine coefficients in Fourier expansions of Q_x, Q_y, equations (48)
$\mathbf{p}(\mathbf{v}, \Omega)$	left-hand side of equation (17)
P	total number of degrees of freedom
P_N	number of degree of freedom associated with the motion dependent forces $\mathbf{f}_N$
P_L	$= P - P_N$
P_x, P_y, P_{xk}, P_{yk}	unbalance forces at U (Figure 4), U_k (Figure 2(b)), equations (1) (N)
q_x^s, q_y^s	sine coefficients in Fourier expansions of Q_x, Q_y, equations (48)
q_{xr}, q_{yr}	modal co-ordinates for vibration in xz and yz planes respectively, equation (54)
$\mathbf{q}$	vector of modal co-ordinates $q_1 \cdots q_H$, equation (23)
$\mathbf{q}_E$	vector of modal co-ordinates of equilibrium periodic solution, equation (30)
Q_R, Q_T	radial and tangential squeeze film forces on journal (N)
Q_x, Q_y	Cartesian components of squeeze film forces on J in Figure 4 (N)
Q_{xi}, Q_{yi}	Cartesian components of squeeze film forces on J_i in Figure 2(a) (N)
$\bar{Q}_x$, $\bar{Q}_y$	mean terms in Fourier expansions of Q_x, Q_y, equations (48)
R	bearing bore (m)
$\mathbf{R}$	receptance matrix, defined by equation (8)
$\mathbf{S}$	matrix defined in equation (14)
$\mathbf{S}_0$	zero frequency value of $\mathbf{S}$
t	time (s)
T	period of rotation ($= 2\pi/\Omega$) (s)
$\mathbf{T}$	matrix defined in equation (14)
$\mathbf{T}_0$	zero frequency value of $\mathbf{T}$
$\mathbf{u}$, $\mathbf{u}_L$, $\mathbf{u}_N$	degrees of freedom vectors, defined in equation (7)
$\mathbf{u}_E$	equilibrium periodic solution, equation (30)
$\mathbf{u}_{HE}$	vector of RHB responses at H degrees of freedom, equations (44a, b)
$\tilde{\mathbf{u}}$	complex amplitude of $\mathbf{u}$ for $\mathbf{u}$ harmonic
$\mathbf{u}_C$, $\mathbf{u}_S$	cosine and sine coefficient vectors of $\mathbf{u}$ for $\mathbf{u}$ harmonic, equation (9a)
$\bar{\mathbf{u}}$, $\mathbf{u}_C^s$, $\mathbf{u}_S^s$	Fourier coefficient vectors of $\mathbf{f}$, equation (12a)
U, U_k	unbalance at U (Figure 4), U_k (Figure 2(b)), equations (1) (kg m)
$\mathbf{U}(\tau)$	periodic matrix defined in equation (39a)
$\mathbf{v}$	vector of unknown Fourier coefficients in $\bar{\mathbf{h}}$, $\mathbf{h}_C^s$, $\mathbf{h}_S^s$
$\mathbf{v}_{aug}$	vector defined in equation (20)
$\mathbf{V}(\tau)$	periodic matrix defined in equation (39b)
$\mathbf{w}$	vector of perturbations in $\mathbf{q}$, $\mathbf{q}'$, equation (36)
W	equivalent static load on squeeze film, equation (63) (N)
$\mathbf{W}(\tau)$	periodic matrix defined in equation (38)
$\mathbf{W}_k$	matrix defined in equation (40)
X_{B_i}, Y_{B_i}, X_{J_i}, Y_{J_i}	displacements of B_i, J_i (m)
X_J, Y_J, X_P, Y_P	displacements of journal J and position P (m)
$\bar{X}_J$, $\bar{Y}_J$, $\bar{X}_P$, $\bar{Y}_P$	mean terms in Fourier expansions of X_J, Y_J, X_P, Y_P respectively
z	axial co-ordinate (m)
$\{z_{ij}(\omega)\}$	impedance matrix, equation (59)
$\mathbf{z}$	vector of perturbations in $\mathbf{q}$, equation (33)
$\alpha_{ij}(\omega)$, $\beta_{ij}(\omega)$	x, y receptances between positions i and j (m/N)

δ_{Ns}	constant defined in equation (51)
ε	non-dimensional eccentricity of J from B $= e/c$
ε_{0xJ}, ε_{0yJ}	non-dimensional x, y static misalignments of J ($= e_{0xJ}/c$, e_{0yJ}/c)
θ	angular position measured from maximum film thickness position (rad)
ψ	attitude angle (rad)
ψ^r_{xi}, ψ^r_{yi}	mass normalized mode shapes at position i in x, y directions ($\mathrm{kg}^{-0\cdot 5}$)
Ψ^h	mass normalized mode shape vector
ϕ_k	phase shift of unbalance at U_k (Figure 2(b)), equations (1) (rad)
λ_l	leading eigenvalue of **M** or leading Floquet multiplier
η	dynamic viscosity of oil ($\mathrm{N\,s/m^2}$)
τ	$= \varpi t$, non-dimensional time
ϖ	fundamental frequency of receptance harmonic balance solution (rad/s)
ω	general frequency (rad/s)
ω_0	natural frequency used to non-dimensionalize equation (18) (rad/s)
ω_h	undamped natural frequency in mode $h = 1 \cdots H$ (rad/s)
ω_{xr}, ω_{yr}	undamped natural frequencies of mode r and xz and yz planes (rad/s)
σ	arc-length parameter
Ω	rotor rotational speed (rad/s)
Γ	period of harmonic balance periodic cycle ($= NT$) (s)
$(\ )^R$, $(\ )^I$	applied to matrix: real and imaginary parts of ( ) respectively
$(\ )^{\mathrm{T}}$	applied to matrix, vector ( ): transpose of ( )
( )	d( )/dt
$(\ )'$	d( )/dτ